Aerospace Science and Technology 158 (2025) 109908

Contents lists available at ScienceDirect

Aerospace Science and Technology

journal homepage: www.elsevier.com/locate/aescte

Advanced aerodynamic analysis of the supersonic flow field of an aerospike engine ☆

Luca Fadigati [a,*], Ernesto Sozio [c], Federico Rossi [c], Nabil Souhair [a,b], Fabrizio Ponti [a]

[a] University of Bologna, Department of Industrial Engineering, Via Fontanelle, 40, Forlì, 47121, Italy
[b] International University of Rabat, Aerospace and Automotive Engineering School, Sala al Jadida, Rabat, 11100, Morocco
[c] Pangea Aerospace, Avinguda Número 1, 20-1st floor, Barcelona, 08040, Spain

ARTICLE INFO

Communicated by Damiano Casalino

Keywords:
Aerospike
Compressible supersonic flow
Shape optimization
Prandtl-Meyer expansion

ABSTRACT

In the last decade, the aerospike has been reconsidered as an alternative of the traditional bell-shaped nozzle because with the improving of additive manufacturing technique it has been possible to enable the fabrication of complex features while drastically reduce production time and manufacturing costs. Nevertheless, there are still some issue that should be solved to realize reliable engines. During the ascent phase of a launcher, the aerospike could deliver more thrust than a bell-shaped nozzle with the same expansion ratio and exit section area due to the capability to adapt the expansion reaching the ambient pressure in a wide range of altitudes. This research has been focused on the improvement of the aerospike performance simulating a small engine with different spike shapes in order to identify sources of losses and to determine which is the most efficient one. The considered shapes have been obtained using the Angelino's method and cutting the spike to achieve the target base radius. The exit section has been kept constant in different designs. The study compares the simulations results with the ones obtained applying the isentropic nozzle theory, highlighting the different behaviours of the flow at throat section and over the spike in terms of pressure and velocity distribution. In particular, the influence of both the round connection between the throat section and the external wall, and the connection between flow inclination at the throat section and the thrust loss at the base has been analyzed. Finally, a rough estimation of the thrust-to-mass ratio has been obtained.

1. Introduction

During the launcher ascent, the aerospike engines can deliver higher thrust than a bell-shaped nozzle with the same expansion ratio and exit section area, because the aerospike can adapt the gas expansion working in optimal expansion condition for a large ambient pressure range [1,2]. The bell-shaped nozzle only works in optimal expansion at one ambient pressure, hence at one altitude, while during most of the flight, it works almost in non-optimal conditions delivering less thrust with respect to an aerospike. In addition, the bell-shape nozzles have the limitation related to the formation of a normal shock-wave inside the divergent section when the expansion ratio is much lower than the optimal one. This leads to a limit on the maximum design expansion ratio that could be used at lower altitudes. Despite the aerospike engine overcoming these drawbacks, it has been abandoned because its manufacturing was too expensive and the design of the cooling system was too challenging. Nowadays, the additive manufacturing techniques allow to overcome these issues, as the work of several research groups and companies is demonstrating. For example, Schwarzer-Fischer which proposed a ceramic additive manufacturing method to build the entire engine [3]; Pangea Aerospace [4–6] is working with Aenium [7,8] to build a low-cost additively manufactured reusable aerospike engine designed to produce a thrust in the order of 300 kN at sea level. In [9], Tian has tested and simulated and an aerospike nozzle in a hybrid rocket

☆ This document is the results of the research project in collaboration with Pangea Aerospace.

* Corresponding author.
E-mail addresses: luca.fadigati2@unibo.it (L. Fadigati), ernesto.sozio@pangeaaerospace.com (E. Sozio), federico.rossi@pangeaaerospace.com (F. Rossi), nabil.souhair@uir.ac.ma (N. Souhair), fabrizio.ponti@unibo.it (F. Ponti).
URLs: https://www.unibo.it/sitoweb/luca.fadigati2, https://www.linkedin.com/in/luca-f-543930256 (L. Fadigati), https://www.linkedin.com/in/ernesto-sozio-a166a285 (E. Sozio), https://www.linkedin.com/in/federico-rossi-3abb41147/ (F. Rossi), https://www.linkedin.com/in/nabil-souhair-phd-80b70ba9/ (N. Souhair), https://linkedin.com/in/fabrizio-ponti-70a93222 (F. Ponti).

https://doi.org/10.1016/j.ast.2024.109908
Received 14 May 2024; Received in revised form 2 December 2024; Accepted 21 December 2024

Available online 31 December 2024

Nomenclature

Greek Symbols

β	Angle between section normal and engine axis	rad
δ	Wall slope	rad
$\delta C_{F,j}$	Percentage variation of the thrust coefficient	-
ΔF	Thrust difference with respect to the theoretical one	N
ΔF^{eq}	Thrust difference with respect to the equivalent theoretical thrust	N
$\Delta\dot{m}$	Mass flow rate difference with respect to the theoretical case	kg/s
Δt	Simulation time step	s
Δt_{cc}	Inlet initial transient duration	s
$\Delta\theta_{PM}$	Flow turn angle during the Prandtl-Meyer expansion	rad
Δt_{pp}	Post-processing time interval	s
ϵ	Aspect ratio	-
η_b^{bc}	Ratio between the aerospike base radius (before the cut) and the exit section radius	-
γ	Heat capacity ratio	-
μ	Dynamic viscosity	kg/(m s)
ν	Prandtl-Meyer function	rad
Ω	Control volume	
ω	Specific dissipation rate	s^{-1}
$\partial\Omega$	Boundary of the control volume	
ψ	Cumulative area	m^2
ρ	Flow density	kg/m^3
ρ_w^{eq}	Equivalent wall density	kg/m^3
σ_F	Standard deviation of the engine thrust	N
$\sigma_{\dot{m}}$	Standard deviation of the mass flow rate	kg/s
θ	Angle between flow velocity and engine axis	rad
ξ	Mach angle	rad

Roman Symbols

$\mathcal{A}$	Effective area	m^2
A	Section area	m^2
A_{th}^{eq}	Equivalent throat section area	m^2
A_{th}^{geo}	Geometrical throat section area	m^2
B′	End of the theoretical Prandtl-Meyer expansion	
C_d	Discharge coefficient	-
C_F	Thrust coefficient	-
$C_{F,j}$	Thrust coefficient delivered by the surface j	-
C_p	Specific heat capacity at constant pressure	J/(kg K)
c_s	Speed of sound	m/s
d_e	Aerospike exit section diameter	m
d_h	Distance from the horizontal farfield from the engine axis	m
d_o	Distance from the outlet to the throat section	m
d_v	Distance from the vertical farfield to the throat section	m
r_e	Aerospike exit section radius	m
$\mathbf{F}$	Thrust vector	N
F	Thrust	N
F_j	Thrust delivered by the surface j	N
$\boldsymbol{\mathcal{F}}$	Average momentum flow	N
F^{eq}	Equivalent theoretical thrust	N
h_w^{DemoP1}	DemoP1 spike wall thickness	m
I	Identity matrix	-
I_{sp}	Specific impulse	m/s
k	Turbulent kinetic energy	m^2/s^2
l_{rb}	Recirculating bubble length	m
L_{spike}	Spike axial length (measured from the point J)	m
$L_{\text{spike}}^{\text{bc}}$	Spike axial length before the cut (measured from the point J)	m
$\mathcal{M}$	Molar mass	g/mol
M	Mach number	-
m	Mass	kg
$\bar{m}$	Dimensionless spike and base mass	-
$\dot{m}$	Mass flow rate	kg/s
$\hat{\mathbf{n}}$	Unit normal vector	-
$\hat{\mathbf{n}}_{ea}$	Unit vector parallel to engine axis	-
NPR	Nozzle pressure ratio	-
p	Static pressure	Pa
p_0	Total pressure	Pa
p_{cut}	Percentage of axial length cut from the spike	-
p_r	Relative pressure	Pa
Pr	Prandtl number	-
r	Radial coordinate	m
r_{iw}	Inner surface of the wall radial coordinate	m
r_w	Radial coordinate of the wall	m
r_b^{bc}	Aerospike base radius before the cut	m
r_g	Aerospike external wall radius	m
R_s	Specific gas constant	J/(kg K)
s	Curvilinear coordinate of the wall surface	m
S_j	j-th surface	
$\tilde{s}$	Curvilinear coordinate of the wall inner surface	m
T	Static temperature	K
t	Time	s
T_0	Total temperature	K
$\boldsymbol{\tau}$	Shear stress tensor	Pa
$\mathbf{u}$	Flow velocity	m/s
u	Flow velocity modulus	m/s
V	Volume	m^3

Subscripts

$\hat{\cdot}$	Average value of variable $\cdot$
cc	Combustion chamber
cn	Converging nozzle
eng	Engine
ew	External wall
sb	Spike and base
wss	Wall shear stress
$\underline{\cdot}$	Every underline symbols refers to a simulation result
amb	Ambient condition
ea	Engine axis
l	Left surface of the control volume
r	Right surface of the control volume
th	Throat section
w	Wall surface of the control volume

motor in order to improve the specific impulse and the combustion efficiency in a wider range of throttle conditions. The aerospike nozzle has also been studied, both numerically by Li and Huang in [10,11] and experimentally by Zhu, Z. Ma and D. Shen in [12–14], as nozzle for a rotating detonation engines.

In recent years, the research was also focused on the design optimization to reach the maximum performance, for example Liu has worked on the optimization of the design of an aerospike with rotating detonation [15], Wang has elaborated a simplified design and optimization method of aerospike nozzle contour describing the spike with a parabola [16]. Some research has also been done on the spacing between the nozzles of a clustered plug nozzle [17]. Wang [18,19] is also working on the expansion-deflection nozzle which works similarly to the aerospike because the flow is expanded through a Prandtl-Meyer expansion, therefore is able to adapt the expansion according to the ambient pressure.

Abbreviations

CAD Computer-Aided Design
CEA Chemical Equilibrium with Applications
DLR Deutsches Zentrum für Luft-und Raumfahrt
DMLS Direct Metal Laser Sintering
HLLC Harten, Lax, Van Leer, Contact
LES Large Eddy Simulation
M-VLED Multi-Volume Laser Energy Density
NASA National Aeronautics and Space Administration
RSS Restricted Shock Separation
SSME Space Shuttle Main Engine
SST Shear Stress Transport
SWBLI Shock Wave Boundary Layer Interaction

Some researcher groups are working on the improvement of the additive manufacturing methods because there are still some issues to be overcome. For example, Aenium [7,8] combines the use of Direct Metal Laser Sintering (DMLS) technology with Multi-Volume Laser Energy Density (M-VLED) [20] to dynamically control the laser energy density in order to tailor the local material properties. Specific alloys should be used for the additive manufacturing techniques, for example National Aeronautics and Space Administration (NASA) has developed the alloy called GRCop-42 for regeneratively-cooled combustion chambers and nozzles [21–23]. This material has been chosen for its high strength and high thermal conductivity. In [24], Demeneghi characterizes the alloy GRCop-42 and, in [25] he compares the laser powder bed fusion and the laser powder direct energy deposition analyzing the material porosity, which could be an issue under thermal loads.

The main focus of this work is to investigate how performance is affected by the spike shape keeping fixed the aerospike base and exit section area. The DemoP1 engine, which is a technological demonstrator designed and built by Pangea Aerospace [4–6], has been taken as reference. Its spike has been redesigned according to the method described by Angelino in [26]. Four tested engine geometries have been generated. They differ in length and in the inclination of the wall at the end of the spike. According to the isentropic nozzle theory, these engines should have the same performance because in the ideal case the aerospike base is always able to recover the thrust missing to reach the ideal performance of full spike. But according to [27, p. 8], in over-expanded condition, the base generates small drag or neutral contribution leading to thrust losses. The simulations have been done in over-expanded conditions because, given a fixed expansion ratio, this is the portion of the mission trajectory where the aerospike shows its adaptation capabilities, exceeding the performance of an equivalent bell-shaped nozzle. Also, this is the most interesting condition to investigate the different flow features developing around the spike. The simulations have been done using *dbnsTurbFoam* which is an open-source tool designed to simulate compressible turbulence flows. This solver has been validated by Fadigati [28] with experimental data available in literature [29]. The post-processing analysis has been focused on identifying the source of thrust losses comparing the results with the theoretical one which can be considered as an upper thrust limit. In particular, the flow behaviour at the throat section has been studied, as well as in the Prandtl-Meyer expansion, which occurs over the initial part of the spike.

2. Numerical approach

The simulations shown in this work have been run following the numerical methodology displayed [28,30], therefore only a brief summary will be explained in this paper. The methodology has been validated in [28,30] with a linear spike fed by compressed air (the experimental results have been obtained from [29]). And additional qualitative validation has been done in [28] with DemoP1 experimental test done at Deutsches Zentrum für Luft-und Raumfahrt (DLR) facility [6]. Due to the high computational cost, an Large Eddy Simulation (LES) has not been run to additionally confirm the results shown in this study. The code *dbnsTurbFoam* has been chosen because it solves the turbulence compressible Navier-Stokes equations coupled with the ideal gas law. This solver implements the Harten, Lax, Van Leer, Contact (HLLC) [31] scheme designed to capture shocks and expansion waves. k-ω Shear Stress Transport (SST), developed by Menter [32,33], has been chosen as turbulence model because it can predict the flow detachment in the boundary layer but at the same time it works well also far away from walls. A chemically frozen composition has been assumed. According to [1], this hypothesis introduces an error in the performance estimation, but the size of the tested shapes is in the same order of magnitude, hence they are affected similarly by the non-equilibrium chemical kinetics. In addition, the performance of the four tested engines will be compared with the isentropic theory, which shares the hypothesis of frozen expansion. Therefore, the performance losses with respect the ideal case will only be a consequence of the fluid viscosity and two-dimensional expansion, i.e. the spike shape. Finally, up to the throat section the flow speed is too slow that the chemical reactions have time to reach the equilibrium condition, while after it, the flow temperature and pressure vary too fast that the equilibrium condition is not reached over the spike. The flow properties, like the specific heat capacity and the molar mass, have been evaluated using the software Chemical Equilibrium with Applications (CEA), developed by NASA to calculate the chemical equilibrium of a mixture [34–36]. For the following tests, it has been assumed the same propellant composition used in [28], which is the propellant composition used by DemoP1: liquid oxygen and liquid methane with an oxidizer to fuel mass ratio of about 2.8. CEA has been used to evaluate the flow properties at the throat section.[1] Tables 1 and 2 report the thermodynamics and transport properties respectively used in all simulations. The parameters ρ_{inlet} and $c_{s_{inlet}}$ are evaluated at the inlet, and they have been used in the inlet boundary conditions, while the other variables with the subscript th are evaluated at the engine throat section. The combustion chamber temperature has been evaluated by CEA: $T_{cc} = 3340\,\mathrm{K}$.

Table 1
Thermodynamic properties obtained by CEA [34–36].

Thermodynamics properties	
p_{th} [MPa]	2.552
T_{th} [K]	3140
$C_{p_{th}}$ [J/(kg K)]	2452
γ_{th} [−]	1.206
$\mathcal{M}_{th}$ [g/mol]	19.84
ρ_{inlet} [kg/m^3]	3.1089
$c_{s_{inlet}}$ [m/s]	1272

Table 2
Transport properties obtained by CEA [34–36].

Transport properties	
μ_{th} [kg/(m s)]	1×10^{-4}
Pr_{th} [−]	0.651
μ_{inlet} [kg/(m s)]	1×10^{-4}

3. Tested spike shapes

One of the aims of this work is to compare different designs of the spike keeping the same base radius r_b and expansion ratio. The tested shapes have been obtained substituting the original DemoP1 spike with the one generated by the Angelino's method described in [26] and then cutting the spike in order to obtain the same base radius of DemoP1. Fig. 1 shows the uncut spike which is coloured grey, while the cut one is coloured black. Four geometries have been created varying the η_b^{bc} parameter which is the ratio between r_b^{bc}, the base radius before doing

[1] *dbnsTurbFoam* can handle only one fluid, hence a chemically frozen composition with a fluid that has the properties evaluated by CEA at throat section has been simulated.

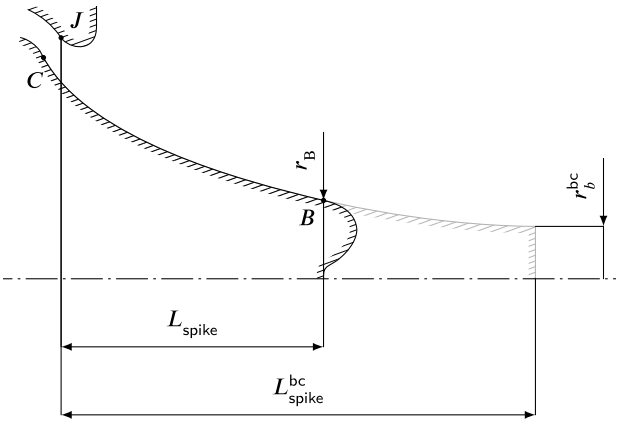

Fig. 1. Engine shape parameters.

the cutting operation, and the exit section radius. As shown in Fig. 2, the point C of the spike has been smoothly connected to the points D using a Bézier curve with three control points in order to ensure the continuity of the wall and its first derivative. This type of curve has been chosen because it is usually used to acquire a more control of the wall contour; its extension, called B-spline, has been used by Wang in [19] to design the pintle wall. An analogue operation has been done at the spike end to connect it to the original base of DemoP1. Hence, a Bézier curve with three control points has been added between the point B and the base tip.[2] The characteristic parameters of the four tested geometries are listed in Table 3 in which p_{cut} is the axial length of the cut portion of the spike in percentage.

$$\eta_b^{bc} = \frac{r_b^{bc}}{r_e} \tag{1}$$

$$p_{cut} = 1 - \frac{L_{spike}}{L_{spike}^{bc}} \tag{2}$$

L_{spike}^{bc} is the axial spike length before doing the cutting operation while L_{spike} is the axial spike length after the cut. The spike length is measured axially from the point J to the point B. The point J has been chosen because it is the point from which the expansion fan starts. η_b^{bc} is bounded between 0.00 and 0.33 because negative values of η_b^{bc} are meaningless, while at $\eta_b^{bc} = 0.33$, the base radius is already equal to the original DemoP1 one. Higher values of η_b^{bc} will produce spikes that are always at higher radial coordinates than DemoP1 base, hence it is not possible to cut them obtaining the required base radius. The case A corresponds to the original DemoP1 spike shape which is shown in Fig. 2 with the surface names highlighted. Despite that the point C is the same for the four geometries, the wall inclination in C varies with η_b^{bc} leading to small variations in the DC segment and hence in the throat area as reported in the last column of Table 3. The geometrical throat segment has been identified by the shortest line between the upper and lower curves shown in Fig. 3. The throat sections are represented in Fig. 4 with the line J′C′, where in every case, the point J′ coincides with J, while the point C′ changes its location along the DC line: in Fig. 4 the geometrical throat sections cannot be distinguished because they are almost overlapping.

According to the literature knowledge, the aerospike base can not recover the thrust delivered by the missing part of the spike in overexpansion [27, p. 8]. In this condition, theoretically, the flow reaches the ambient pressure over the spike, therefore the base recovers thrust aligning the flow with the engine axis. Changing the η_b^{bc} parameter, different spike shapes have been drawn. For low values of η_b^{bc}, the flow

[2] The base tip is the point of the base with the highest axial coordinate.

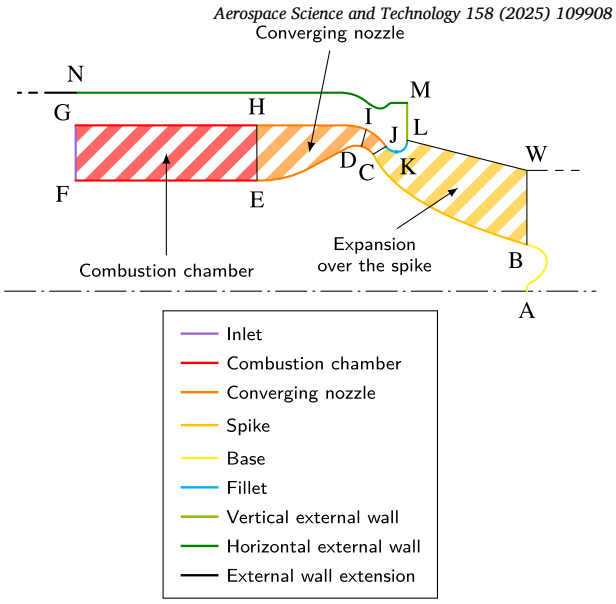

Fig. 2. DemoP1 surfaces and subdomains.

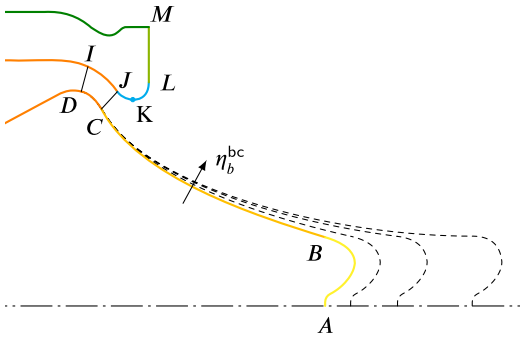

Fig. 3. Different spike designs following Angelino's method [26]: the coloured spike is the original DemoP1 shape.

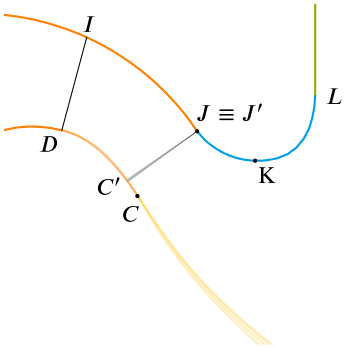

Fig. 4. Magnification of the different spike design throat section.

leaves the spike with higher inclination towards the engine axis, hence the base should recover more thrust to reach the ideal performance, which implies possible higher losses. While for high values of η_b^{bc}, the flow leaves the spike almost axially. Therefore, the base should generate zero thrust and the losses should be almost zero. A second phenomenon need to be considered. In front of the base, there is a recirculating bubble. For low values of η_b^{bc}, its size is small because the flow leaves the spike pointing towards the engine axis, while for high values, the recirculating bubble size grows leading to thrust oscillation and maybe additional losses due to low pressure at the base. Finally, increasing η_b^{bc}, the spike becomes heavier. Therefore, a priori, it is complicated to pre-

Table 3
Parameters used to create the new DemoP1 spike using the Angelino's method [26].

	Angelino's method parameters					
Case name	r_b^{bc} [mm]	η_b^{bc} [−]	p_{cut} [−]	L_{spike}^{bc} [mm]	L_{spike} [mm]	A_{th}^{geo} [mm^2]
A	0	0.00	0.62	181	69	32.49
B	15	0.22	0.45	139	77	32.55
C	20	0.30	0.25	123	93	32.61
D	23	0.33	0.00	117	117	32.64

dict which configuration gives the best performance because varying the η_b^{bc} parameter because there are involved two phenomena with opposite effects on thrust.

4. Simulation settings

The simulation settings are almost identical to the one shown in [28], hence in this section only a brief summary is presented. The simulation domain has been sized according to the literature [37–39] as discussed also in [28]. Fig. 5 shows the domain size and the boundary names. To reduce the computational effort, a 2D axisymmetric simulation has been set. Inside the combustion chamber and the converging nozzle, the mesh is a structured one because the flow direction is known, while outside an unstructured mesh has been used. A structured mesh refinement close to the walls has been used to capture the flow boundary layer. The mesh grows towards the farfields to dissipate vortices, avoiding the back flow phenomenon re-entering into the numerical model, and also to limit the total number of cells. The size of the refinement region over the spike has been adapted to enclose the high-speed flow without wasting cells in the outer region. The mesh size has been chosen according to the mesh convergence study performed in [28]. The used meshes have a number of cells that spans between 52k and 57k: these values are lower than the one used in [28] because in this work over-expanded conditions have been simulated, hence the expansion is confined near the spike, which means that the refinement region over the spike gets smaller. Fig. 6 shows the mesh of the case A. The flow properties are the same shown in Tables 1 and 2. At the inlet, green line in Fig. 5, the total pressure and the temperature rise from the ambient value up to 45 bar (4.5 MPa) and 3340 K respectively which are the DemoP1 combustion chamber design conditions. The total pressure increases linearly in $\Delta t_{cc} = 33$ ms while the temperature grows following a fourth degree polynomial. On every wall, the no-slip and adiabatic conditions have been set. At the farfields, an ambient temperature of 288.15 K has been fixed, while for the ambient pressure a value such that the $NPR = 7.5$ has been chosen in order to simulate an aerospike that is working in over-expanded conditions. Fixed values of k and ω have been set at the inlet and at the farfields, while on the walls the mesh has been refined to have cell sizes in the order of the buffer layer. This allows to use the wall functions as boundary condition for k and ω. The simulations end at $t = 70$ ms, this end-time value has been chosen because it allows to reach the quasi-steady state conditions after the initial transient which ends at 33 ms. In the post-processing of every simulation, the quasi-steadiness of the solution has been checked and the quasi-steadiness in terms of thrust will be shown in Section 5. This set of simulations has been run on a workstation with a Xeon W-3365. The choice to use 16 cores out of 32 available comes from a speedup analysis shown in Fig. 7: the speedup diverges early from the ideal one, therefore 16 cores have been chosen as a compromise between simulation execution time and an efficient use of the available computational power.

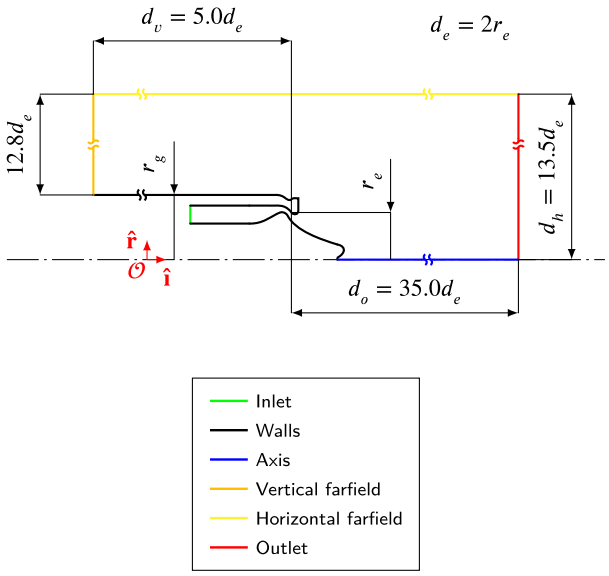

Fig. 5. Domain and boundaries of DemoP1 simulation: r_e is the engine exit section radius while r_g is the engine external wall radius. (For interpretation of the colours in the figure(s), the reader is referred to the web version of this article.)

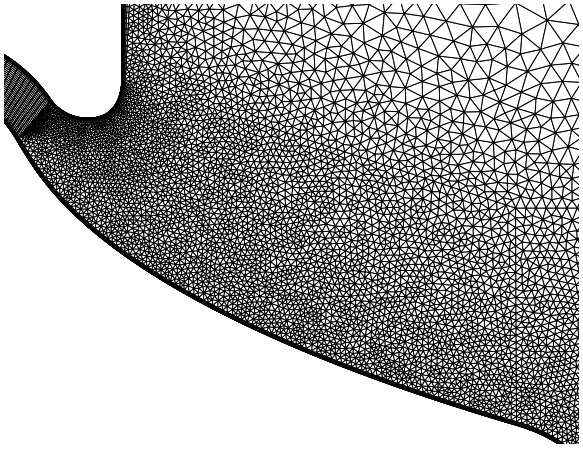

Fig. 6. Magnification of the mesh in the expansion over the spike of the case A.

5. Results

5.1. Thrust coefficient and specific impulse comparison

5.1.1. Simulation post-processing methodology

The code *dbnsTurbFoam* is an unsteady state solver, hence also the simulation results are not steady, therefore in the post-processing phase pressure, temperature and velocity field have been averaged between 60 ms and 70 ms. This interval has been chosen to avoid the effect of the initial transient. In this section, every value must be considered as an average one calculated on the previous time interval unless otherwise specified. The standard deviations reported in the following tables have been evaluated over the same time interval. The variables obtained by the simulations have been underlined as also described in the nomenclature.

In every simulation, the thrust $\underline{F}$ has been evaluated using the following formula

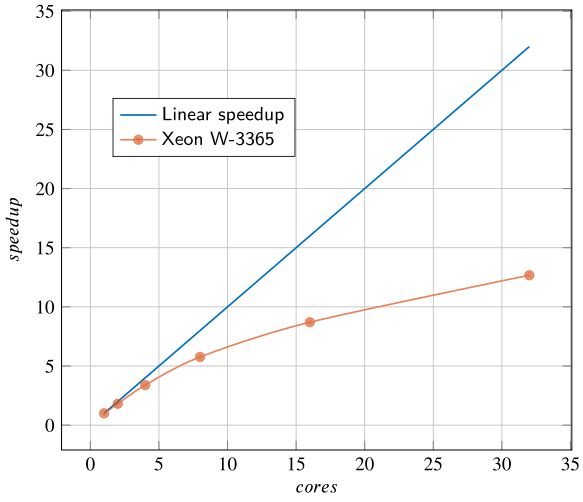

Fig. 7. Simulation speedup on Xeon W-3365.

$$\underline{F} = \underline{F}_{\text{inlet}} + \underline{F}_{\text{walls}} \tag{3}$$

where $\underline{F}_{\text{inlet}}$ is the thrust produced by the part of the engine before the simulation inlet while $\underline{F}_{\text{walls}}$ is the thrust obtained from the pressure and viscous contributions acting on the walls. $\underline{F}_{\text{inlet}}$ can be evaluated similarly as it is done in the isentropic nozzle theory considering the engine inlet like a nozzle exit section:

$$\underline{F}_{\text{inlet}} = \hat{\mathbf{n}}_{ea} \cdot \int_{S_{\text{inlet}}} \left[\underline{\rho}\,\underline{\mathbf{u}} \left(\underline{\mathbf{u}} \cdot \hat{\mathbf{n}} \right) + \left(\underline{p} - p_{amb} \right) \hat{\mathbf{n}} \right] dA \tag{4}$$

where $\hat{\mathbf{n}}_{ea}$ is the unit vector aligned with the engine axis and pointing towards the engine inlet, $\hat{\mathbf{n}} = -\hat{\mathbf{i}}$ is the unit normal vector, S_{inlet} is the inlet surface, $\underline{\rho}$ is the flow density, $\underline{\mathbf{u}}$ is the flow velocity, $\underline{p}$ is the static pressure and p_{amb} is the ambient pressure. $\underline{F}_{\text{walls}}$ can be evaluated as the integral of the pressure and wall shear stress over the engine walls:

$$\underline{F}_{\text{walls}} = \hat{\mathbf{n}}_{ea} \cdot \int_{S_{\text{walls}}} \left[\left(\underline{p} - p_{amb} \right) \mathrm{I} + \underline{\boldsymbol{\tau}} \right] \hat{\mathbf{n}}\, dA \tag{5}$$

where S_{walls} is the union of all wall surfaces excluded the external wall extension that has been added to the engine only to locate the vertical farfield faraway from it. $\underline{\boldsymbol{\tau}}$ is the stress tensor and $\hat{\mathbf{n}}$ is the outward surface normal unit vector. The thrust reduction related to the wall shear stress contribution is evaluated as follows

$$\underline{F}_{\text{wss}} = \hat{\mathbf{n}}_{ea} \cdot \underline{\mathbf{F}}_{\text{wss}} = \int_{S_{\text{walls}}} \hat{\mathbf{n}}_{ea} \cdot \underline{\boldsymbol{\tau}} \hat{\mathbf{n}}\, dA \tag{6}$$

The thrust coefficient of a generic force $\underline{F}_j$ can be obtained using the following formula

$$\underline{C}_{F,j} = \frac{\underline{F}_j}{A_{th}^{geo}\, p_{0,\text{cc}}} \tag{7}$$

where A_{th}^{geo} is the throat area. The average specific impulse has been evaluated averaging the instantaneous specific impulse in the time interval that extends from 60 ms to 70 ms.

5.1.2. Theoretical background

The results extracted from the simulations are compared with the theoretical ones obtained applying the isentropic nozzle theory. The simulation results and the theoretical one have been obtained supposing the frozen expansion hypothesis, hence this comparison is consistent, and it can highlight the losses related to fluid viscosity and the one related to the engine shape. The first reference is an ideal engine which always works in optimal expansion conditions, and it has the same throat section area of DemoP1. Its thrust coefficient, its thrust and the thrust difference are evaluated as follows

$$C_F = \sqrt{\frac{2\gamma^2}{\gamma - 1} \left(\frac{2}{\gamma + 1} \right)^{\frac{\gamma+1}{\gamma-1}} \left[1 - \left(\frac{p_{amb}}{p_{0,\text{cc}}} \right)^{\frac{\gamma-1}{\gamma}} \right]} \tag{8}$$

$$F = C_F\, p_{0,\text{cc}}\, A_{th}^{geo} \tag{9}$$

$$\Delta F = \underline{F} - F \tag{10}$$

Its theoretical specific impulse is obtained using the following equation

$$I_{sp} = \sqrt{\frac{R_s T_{0,\text{cc}}}{\gamma}}\, C_F \left(\frac{\gamma + 1}{2} \right)^{\frac{\gamma+1}{2(\gamma-1)}} \tag{11}$$

The theoretical mass flow rate can be obtained using Equation (12):

$$\dot{m} = \frac{\sqrt{\gamma}\, p_{0,\text{cc}}\, A_{th}^{geo}}{\sqrt{R_s T_{0,\text{cc}}}} \left(\frac{2}{\gamma + 1} \right)^{\frac{\gamma+1}{2(\gamma-1)}} \tag{12}$$

The second reference is an ideal nozzle that always works in optimal expansion conditions, and it has the same mass flow rate of the simulated engine. This comparison allows to remove the penalization due to the mass flow rate reduction related to the fluid viscosity. An equivalent throat section area has been evaluated using the isentropic nozzle theory

$$A_{th}^{eq} = \frac{\underline{\dot{m}}}{p_{0,\text{cc}}} \sqrt{\frac{R_s T_{0,\text{cc}}}{\gamma}} \left(\frac{\gamma + 1}{2} \right)^{\frac{\gamma+1}{2(\gamma-1)}} \tag{13}$$

where $\underline{\dot{m}}$ is evaluated from the simulation. The theoretical thrust can be calculated using the following formula

$$F^{eq} = C_F^{eq}\, p_{0,\text{cc}}\, A_{th}^{eq} \tag{14}$$

where $C_F^{eq} = C_F$ because the thrust coefficient, of an ideal nozzle that always works in optimal expansion conditions, depends only on the nozzle pressure ratio. According to Equation (11) also the specific impulse is the same. $F^{eq} < F$ because $A_{th}^{eq} < A_{th}^{geo}$. The thrust difference for this second comparison is

$$\Delta F^{eq} = \underline{F} - F^{eq} \tag{15}$$

5.1.3. Results comparison

Table 4 shows the mass flow rate obtained from the simulation comparing with the theoretical one calculated using Equation (12). The theoretical mass flow rate grows according to the increment of the throat section area. In every simulation, the calculated mass flow rate is lower than the theoretical one due to the boundary layer. The discharge coefficient is almost equal to 0.988, meaning that the theoretical mass flow rate is reduced by 1.2%.

Table 5 reports the thrust delivered by every tested engine compared with the first ideal reference engine. Increasing η_b^{bc}, the theoretical thrust F increases due to increment of $\dot{m}$, but the same does not happen on the thrust evaluated from the simulation which decreases. The losses related to the wall shear stress increase slightly increasing η_b^{bc} because the engine surface extension increases, but they can not justify the thrust performance detriment compared to the theoretical results. The second comparison, with an ideal engine that has the same mass flow rate evaluated from the simulation, is shown in Table 6. The equivalent throat section area A_{th}^{eq} increases according to the $\dot{m}$ increment. Also, ΔF^{eq} decreases if η_b^{bc} increases. $\Delta F^{eq} < \underline{F}_{\text{wss}}$, hence also in this case the shear stress drag can justify only a portion of the thrust detriment. This additional thrust loss must be related to the pressure distribution. The same result shown in Table 5 has been reported in Table 7 in terms of thrust coefficient to show a fair comparison between different engines which have slightly different throat sections.

Fig. 8 compares thrust coefficients obtained from the simulations with the one calculated from the isentropic nozzle theory. Increasing

Table 4
Summary of the results obtained by simulations in terms of mass flow rate with the spike designed using Angelino's method.

Case	η_b^{bc} [−]	A_{th}^{geo} [cm^2]	$\underline{\dot{m}}$ [kg/s]	$\sigma_{\underline{\dot{m}}}$ [g/s]	$\dot{m}$ [kg/s]	$\Delta\dot{m}$ [kg/s]	C_d [−]
A	0.00	32.49	7.935	0.052	8.028	-0.093	0.988
B	0.22	32.55	7.951	0.146	8.044	-0.093	0.988
C	0.30	32.61	7.962	0.288	8.059	-0.097	0.988
D	0.33	32.64	7.964	0.210	8.066	-0.103	0.987

Table 5
Comparison of the thrust calculated from the simulations and the reference ideal engine that always works in optimal expansion condition, and it has the same throat section of DemoP1.

Case	η_b^{bc} [−]	A_{th}^{geo} [cm^2]	$\underline{F}$ [kN]	$\underline{F}_{wss}$ [N]	$\sigma_{\underline{F}}$ [N]	F [kN]	ΔF [N]
A	0.00	32.49	17.181	-114.5	50	17.537	-356
B	0.22	32.55	17.184	-115.1	34	17.572	-388
C	0.30	32.61	17.176	-115.2	61	17.605	-429
D	0.33	32.64	17.149	-121.6	98	17.621	-472

Table 6
Comparison of the thrust calculated from the simulations and the reference ideal engine that always works in optimal expansion condition, and it has the mass flow rate calculated from the simulations.

Case	η_b^{bc} [−]	A_{th}^{eq} [cm^2]	$\underline{F}$ [kN]	$\underline{F}_{wss}$ [N]	$\sigma_{\underline{F}}$ [N]	F^{eq} [kN]	ΔF^{eq} [N]	$\Delta F^{eq} - F_{wss}$ [N]
A	0.00	32.11	17.181	-114.5	50	17.333	-152	-37
B	0.22	32.18	17.184	-115.1	34	17.370	-186	-70
C	0.30	32.22	17.176	-115.2	61	17.393	-217	-101
D	0.33	32.23	17.149	-121.6	98	17.397	-248	-126

Table 7
Summary of the results obtained by simulations in terms of thrust coefficient with the spike designed using Angelino's method.

Case	η_b^{bc} [−]	A_{th}^{geo} [cm^2]	$\underline{C_F}$ [−]	$\underline{C_{F_{wss}}}$ [−]	$\sigma_{\underline{C_F}}$ [−]	C_F [−]	ΔC_F [−]
A	0.00	32.49	1.175	-0.008	0.003	1.200	-0.024
B	0.22	32.55	1.173	-0.008	0.002	1.200	-0.026
C	0.30	32.61	1.170	-0.008	0.004	1.200	-0.029
D	0.33	32.64	1.168	-0.008	0.007	1.200	-0.032

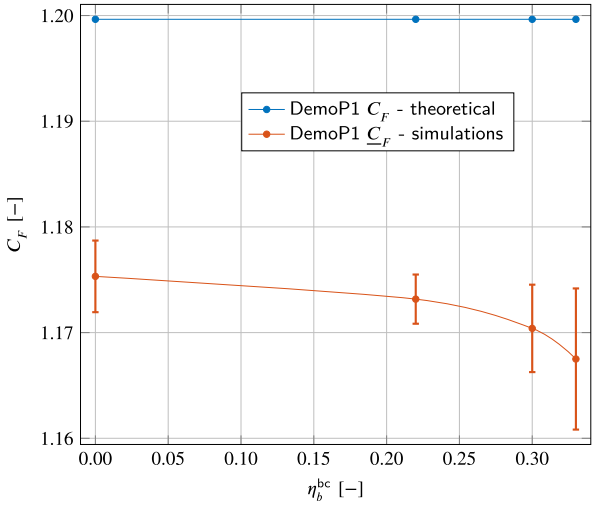

Fig. 8. Thrust coefficient at different η_b^{bc} values compared with the theoretical one. The error bars represent the standard deviation of the thrust coefficient.

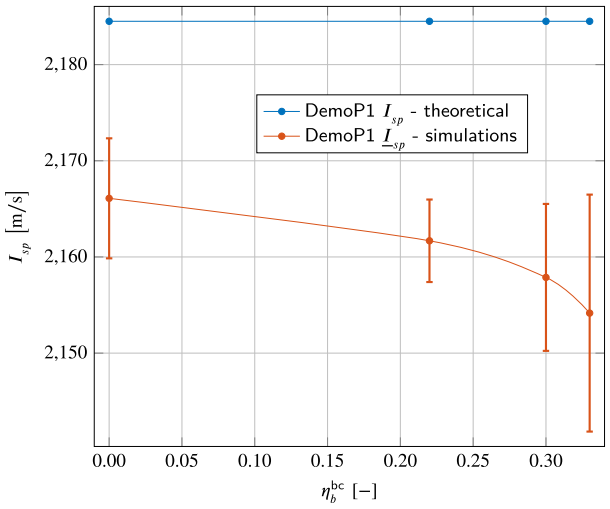

Fig. 9. Specific impulse at different η_b^{bc} values compared with the theoretical one. The error bars represent the standard deviation of the specific impulse.

η_b^{bc}, the thrust coefficient decreases, while its standard deviation increases: the latter phenomenon will be discusses in Section 5.6. As shown in Fig. 9, in similar way the specific impulse decreases if η_b^{bc} increases. This decrement is related to the decreasing thrust and increasing mass flow rate. Hence, in conclusion, the engine should have the lowest η_b^{bc} to maximize the thrust coefficient and the specific impulse, reducing also the thrust oscillations.

5.2. Thrust delivered by every surface

5.2.1. Simulation post-processing methodology

An additional investigation has been done to identify the thrust contributions due to pressure and viscous forces distributed on each surface. Fig. 10 shows the regions in which the engine has been divided highlighting the surfaces interested in this analysis. For every surface, a theoretical thrust contribution has been calculated and compared with

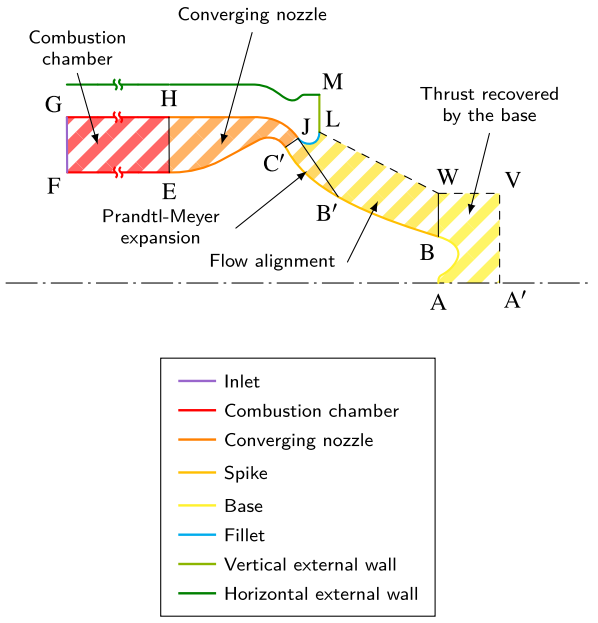

Fig. 10. Subdivision of the engine in five regions used to evaluate the thrust produced by every surface. (For interpretation of the colours in the figure(s), the reader is referred to the web version of this article.)

the one evaluated from the simulation. In every simulation, for the j-th surface, the thrust is calculated using the Equation (16):

$$\underline{F}_j = \hat{\mathbf{n}}_{ea} \cdot \int_{S_{\text{wall},j}} \left[\left(\underline{p} - p_{amb} \right) \mathrm{I} + \underline{\boldsymbol{\tau}} \right] \hat{\mathbf{n}} \, dA \tag{16}$$

where $S_{\text{wall},j}$ is the j-th wall surfaces highlighted in Fig. 10. The external wall extension, black lines in Fig. 2, has not been considered because it is not part of the engine. It has been added only to shift the vertical farfield far away from the engine.

The inlet contribution has been evaluated considering combustion chamber with finite cross-section area. The part of the engine before the inlet has been considered like an ideal nozzle that has the inlet surface as exit section with an inviscid flow. Therefore, Equation (4) has been used. The thrust coefficient related to the j-th surface is calculated using Equation (7). As discussed in Section 5.1, also in this section every value has been averaged within the time interval between 60 ms and 70 ms.

5.2.2. Theoretical thrust delivered by individual surface

The isentropic nozzle theory has been used to evaluate the theoretical thrust of every surface. For the inlet surface, the theoretical thrust has been evaluated substituting the isentropic nozzle theory results into Equation (4) obtaining

$$F_{\text{inlet}} = \dot{m} u_{\text{inlet}} + \left(p_{\text{inlet}} - p_{amb} \right) A_{\text{inlet}} \tag{17}$$

The engine has been divided in five regions as shown in Fig. 10: combustion chamber, converging nozzle, Prandtl-Meyer expansion, remaining part of the spike and the wake. The theoretical thrust provided by each region can be evaluated applying the integral momentum equation combined with the isentropic nozzle theory. Considering a generic engine section like the one shown in Fig. 11, the momentum equation can be integrated over the control volume Ω and, according to the isentropic nozzle theory, the flow is inviscid and the time derivative is set to zero due to the steady state hypothesis.

$$\oint_{\delta\Omega} \rho \mathbf{u} \left(\mathbf{u} \cdot \hat{\mathbf{n}} \right) dS = \oint_{\delta\Omega} -p \hat{\mathbf{n}} \, dS \tag{18}$$

The integrals of Equation (18) can be split in three boundary control volume surfaces: the left S_l, the right S_r and the wall S_w surfaces. The

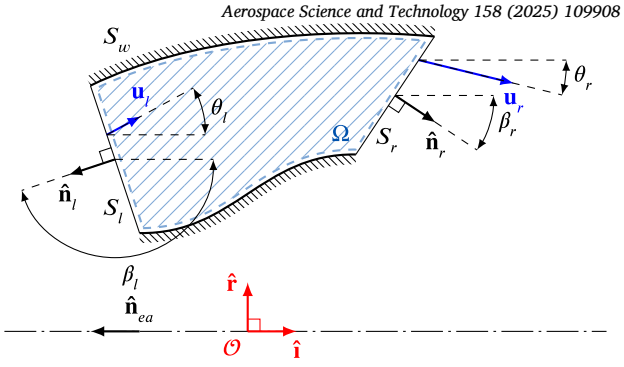

Fig. 11. Sketch of a generic engine section.

term $\oint_{\delta\Omega} p_{amb} \hat{\mathbf{n}} \, dS = \mathbf{0}$ can be added to the right side to highlight the relative pressure.

$$\int_{S_l \cup S_r \cup S_w} \rho \mathbf{u} \left(\mathbf{u} \cdot \hat{\mathbf{n}} \right) dS = \int_{S_l \cup S_r \cup S_w} -\left(p - p_{amb} \right) \hat{\mathbf{n}} \, dS \tag{19}$$

According to the isentropic nozzle theory, the walls cannot be crossed by the flow, hence $\int_{S_w} \rho \mathbf{u} \left(\mathbf{u} \cdot \hat{\mathbf{n}} \right) dS = \mathbf{0}$, and every variable is constant over S_l and S_r. Finally, the thrust is defined as $\mathbf{F} = \int_{S_w} \left(p - p_{amb} \right) \hat{\mathbf{n}} \, dS$:

$$\begin{aligned} &\rho_l \mathbf{u}_l \left(\mathbf{u}_l \cdot \hat{\mathbf{n}}_l \right) A_l + \rho_r \mathbf{u}_r \left(\mathbf{u}_r \cdot \hat{\mathbf{n}}_r \right) A_r = \\ &- \left(p_l - p_{amb} \right) \hat{\mathbf{n}}_l A_l - \left(p_r - p_{amb} \right) \hat{\mathbf{n}}_r A_r - \mathbf{F} \end{aligned} \tag{20}$$

where A_l and A_r are the surface area of S_l and S_r respectively, p_{amb} is the ambient pressure. The walls cannot be crossed by the flow, therefore the mass flow rate at the left surface is equal to the one at the right surface: $\dot{m} = -\rho_l \left(\mathbf{u}_l \cdot \hat{\mathbf{n}}_l \right) A_l = \rho_r \left(\mathbf{u}_r \cdot \hat{\mathbf{n}}_r \right) A_r$. The thrust is projected along the engine axis.

$$\begin{aligned} F = \hat{\mathbf{n}}_{ea} \cdot \mathbf{F} = \; & \dot{m} \left(\hat{\mathbf{n}}_{ea} \cdot \mathbf{u}_l - \hat{\mathbf{n}}_{ea} \cdot \mathbf{u}_r \right) \\ & - \left(p_l - p_{amb} \right) \hat{\mathbf{n}}_{ea} \cdot \hat{\mathbf{n}}_l A_l \\ & - \left(p_r - p_{amb} \right) \hat{\mathbf{n}}_{ea} \cdot \hat{\mathbf{n}}_r A_r \end{aligned} \tag{21}$$

Differently from the traditional isentropic nozzle theory, the nozzle sections are not perpendicular to the engine axis and the flow is not axial. Therefore, as shown in Fig. 11, the surface unit normal vector forms an angle β with the $\hat{\mathbf{i}}$ direction: $\hat{\mathbf{n}}_{ea} \cdot \hat{\mathbf{n}}_l = -\cos\beta_l$ and $\hat{\mathbf{n}}_{ea} \cdot \hat{\mathbf{n}}_r = -\cos\beta_r$; while the flow forms an angle θ with unit vector $\hat{\mathbf{i}}$: $\hat{\mathbf{n}}_{ea} \cdot \mathbf{u}_l = -u_l \cos\theta_l$ and $\hat{\mathbf{n}}_{ea} \cdot \mathbf{u}_r = -u_r \cos\theta_r$. Hence, the thrust delivered by the j-th section becomes

$$\begin{aligned} F_j = \; & \dot{m} \left(u_{r,j} \cos\theta_{r,j} - u_{l,j} \cos\theta_{l,j} \right) \\ & + \left(p_{r,j} - p_{amb} \right) A_{r,j} \cos\beta_{r,j} \\ & + \left(p_{l,j} - p_{amb} \right) A_{l,j} \cos\beta_{l,j} \end{aligned} \tag{22}$$

Equation (22) is valid also for the region over the last part of the spike and the one in front of the base because the points W and V have been chosen in order to contain all the supersonic flow exiting from the engine. Hence, over the lines LW and WV the pressure is supposed to be equal to the ambient one, and the mass flux through these surfaces is zero. Therefore, they do not contribute to the thrust equation.

The next step consists in the estimation of the u, p and θ along the lines GF, HE, JC′, JB′ and JB. From the inlet to the line JB′, the speed and the pressure are evaluated using the isentropic nozzle theory and the Prandtl-Meyer one in the first part of the supersonic expansion. The relation between the local aspect ratio and the Mach number is slightly modified:

$$\epsilon = \frac{\mathcal{A}}{\mathcal{A}_{th}} = \frac{1}{M} \left(\frac{1 + \frac{\gamma-1}{2} M^2}{\frac{\gamma+1}{2}} \right)^{\frac{\gamma+1}{2(\gamma-1)}} \tag{23}$$

$$\mathcal{A} = A \sin \xi \tag{24}$$

where A is the geometrical area of the nozzle section, while ξ is the Mach angle of the flow that crosses the surface. According to the theory, the flow crosses the surface A with an angle equal to ξ. $\mathcal{A}_{th} = A_{th}$ because $\xi_{th} = \frac{\pi}{2}$. The simulated aerospike works in over-expanded conditions, hence the pressure should reach ambient conditions at the end of the Prandtl-Meyer expansion, therefore for the lines after JB′, $p = p_{amb}$ and the flow velocity module becomes constant, but the flow can still change its direction. The flow direction has been supposed to be normal to the lines GF, HE, JC′, while at the Prandtl-Meyer expansion end its inclination is equal to

$$\theta_{\mathrm{JB}'} = \theta_{th} + \Delta\theta_{PM} \tag{25}$$

where θ_{th} is the flow inclination at the throat section (line JC′) and $\Delta\theta_{PM}$ is the angle of which the flow turns due to the Prandlt-Meyer expansion. It can be evaluated using Equations (26) and (27):

$$M_{\mathrm{JB}'} = \sqrt{\frac{2}{\gamma - 1}\left[\left(\frac{p_{0,\mathrm{cc}}}{p_{amb}}\right)^{\frac{\gamma-1}{\gamma}} - 1\right]} \tag{26}$$

$$\Delta\theta_{PM} = \nu\left(M_{\mathrm{JB}'}\right) - \nu\left(M_{th}\right) \tag{27}$$

where $M_{\mathrm{JB}'}$ is the Mach number at the end of the Prandtl-Meyer expansion and $\nu(M)$ is the Prandtl-Meyer function:

$$\nu(M) = \sqrt{\frac{\gamma+1}{\gamma-1}}\tan^{-1}\sqrt{\frac{\gamma-1}{\gamma+1}\left(M^2-1\right)} - \tan^{-1}\sqrt{M^2-1} \tag{28}$$

In the last portion of the spike, the flow is deviated and, according to Onofri [27], in over-expansion conditions at the spike end, its direction θ_{BW} is equal to the spike slope. The theoretical thrust delivered by the fillet and external wall can be calculated using Equation (5) where, according to the isentropic nozzle theory, the pressure is equal to the ambient one and the wall shear stresses are zero due to the flow inviscid hypothesis. Therefore, these two surfaces provide zero thrust in the theoretical case. In over-expansion conditions, the aerospike base has to recover the thrust related to the flow deviation from θ_{BW} to the axial direction: $\theta_{\mathrm{A'V}} = 0.0\,\mathrm{rad}$. The aim of this theory is to evaluate an upper thrust limit which can only be met imposing an axial flow along the segment A′V. The control volume related to the last part of the spike contains also the fillet, but, as mentioned above, the fillet provides zero thrust in the theoretical case, therefore the thrust provided by this region is related to the last part of the spike.

5.2.3. Thrust coefficient per surface comparison

Tables 8 and 9 summarize the comparison between the thrust coefficients calculated from the simulations and the theoretical ones. $\underline{C}_{F,j}$, $C_{F,j}$ are respectively the thrust coefficient calculated from the simulations on the j-th wall and the corresponding theoretical one. $\Delta C_{F,j} = \underline{C}_{F,j} - C_{F,j}$ and $\delta C_{F,j} = \frac{\Delta C_{F,j}}{C_F}$, where C_F is the global theoretical thrust coefficient obtained from Equation (8).

Inlet At the inlet $\Delta C_{F,\mathrm{inlet}}$ is small because the same equation is used for the theoretical and simulated engine. The small difference is related to the lower mass flow rate due to the boundary layer.

Combustion chamber The combustion chamber has a constant crosssection area therefore the flow is not accelerated, hence this engine part theoretically delivers zero thrust, but due to the flow viscosity, it produces a small drag.[3]

[3] The magnitude of the combustion chamber drag is small due to the low flow velocity.

Table 8
Comparison between the theoretical thrust coefficient and the ones obtained from the simulations.

Case		A	B	C	D
Inlet	$\underline{C}_{F,\mathrm{inlet}}$ [−]	3.122	3.116	3.111	3.108
	$C_{F,\mathrm{inlet}}$ [−]	3.127	3.121	3.116	3.113
	$\Delta C_{F,\mathrm{inlet}}$ [−]	−0.005	−0.005	−0.005	−0.005
	$\delta C_{F,\mathrm{inlet}}$ [−]	−0.415	−0.414	−0.419	−0.426
Combustion chamber	$\underline{C}_{F,\mathrm{cc}}$ [−]	0.000	0.000	0.000	0.000
	$C_{F,\mathrm{cc}}$ [−]	0.000	0.000	0.000	0.000
	$\Delta C_{F,\mathrm{cc}}$ [−]	0.000	0.000	0.000	0.000
	$\delta C_{F,\mathrm{cc}}$ [−]	−0.037	−0.035	−0.036	−0.040
Fillet	$\underline{C}_{F,\mathrm{fillet}}$ [−]	−0.059	−0.060	−0.062	−0.063
	$C_{F,\mathrm{fillet}}$ [−]	0.000	0.000	0.000	0.000
	$\Delta C_{F,\mathrm{fillet}}$ [−]	−0.059	−0.060	−0.062	−0.063
	$\delta C_{F,\mathrm{fillet}}$ [−]	−4.923	−5.035	−5.202	−5.253
External wall	$\underline{C}_{F,\mathrm{ew}}$ [−]	−0.0005	0.0001	−0.0006	−0.0001
	$C_{F,\mathrm{ew}}$ [−]	0.000	0.000	0.000	0.000
	$\Delta C_{F,\mathrm{ew}}$ [−]	−0.0005	0.0001	−0.0006	−0.0001
	$\delta C_{F,\mathrm{ew}}$ [−]	−0.040	0.006	−0.050	−0.007

Table 9
Comparison between the theoretical thrust coefficient and the ones obtained from the simulations.

Case		A	B	C	D
Converging nozzle	$\underline{C}_{F,\mathrm{cn}}$ [−]	−2.455	−2.440	−2.450	−2.444
	$C_{F,\mathrm{cn}}$ [−]	−2.504	−2.493	−2.482	−2.476
	$\Delta C_{F,\mathrm{cn}}$ [−]	0.050	0.053	0.032	0.033
	$\delta C_{F,\mathrm{cn}}$ [−]	4.130	4.421	2.634	2.722
Spike (Prandtl-Meyer expansion)	$\underline{C}_{F,\mathrm{spm}}$ [−]	0.473	0.474	0.498	0.498
	$C_{F,\mathrm{spm}}$ [−]	0.461	0.456	0.451	0.448
	$\Delta C_{F,\mathrm{spm}}$ [−]	0.011	0.018	0.047	0.050
	$\delta C_{F,\mathrm{spm}}$ [−]	0.956	1.485	3.959	4.158
Spike (last part)	$\underline{C}_{F,\mathrm{slp}}$ [−]	0.071	0.076	0.077	0.079
	$C_{F,\mathrm{slp}}$ [−]	0.067	0.086	0.105	0.115
	$\Delta C_{F,\mathrm{slp}}$ [−]	0.005	−0.010	−0.028	−0.036
	$\delta C_{F,\mathrm{slp}}$ [−]	0.406	−0.875	−2.355	−3.012
Base	$\underline{C}_{F,\mathrm{base}}$ [−]	0.024	0.008	−0.002	−0.010
	$C_{F,\mathrm{base}}$ [−]	0.049	0.029	0.010	0.000
	$\Delta C_{F,\mathrm{base}}$ [−]	−0.025	−0.021	−0.012	−0.010
	$\delta C_{F,\mathrm{base}}$ [−]	−2.105	−1.761	−0.972	−0.823
Total	$\underline{C}_F$ [−]	1.175	1.173	1.170	1.168
	C_F [−]	1.200	1.200	1.200	1.200
	ΔC_F [−]	−0.024	−0.026	−0.029	−0.032
	δC_F [−]	−2.028	−2.207	−2.441	−2.680

Fillet The theory claims that over the fillet the pressure should be equal to the ambient one, hence it should provide zero thrust. Despite that, in every simulation, the fillet delivers a negative thrust contribution that increases its magnitude with increasing η_b^{bc}. This phenomenon is the consequence non-pointwise expansion which is assumed in the Prandtl-Meyer theory, and it is discussed more in detail in Sections 5.3 and 5.4.1.

External wall The theoretical external wall, which includes both the vertical and the horizontal one, generates no thrust because the external flow should be still and at ambient pressure. In the simulations, this surface produces a small drag due to the flow that is sucked by the aerospike wake. In the case B, this surface provides a positive thrust, this is due to a recirculating bubble located over the horizontal external wall. This phenomenon is not investigated here because its effect on the thrust is almost negligible, and it might be comparable with the simulation uncertainty.

Converging nozzle Surprisingly, the theoretical converging nozzle provides a lower thrust coefficient than the simulated one. This phenomenon is related to the flow inclination and pressure distribution at the throat section. The flow at the throat section has a direction that is

Table 10
Comparison between the theoretical flow direction at the throat section and the averaged one from the simulation results. In the last column, it is reported the error on θ_{JB}.

Case	η_b^{bc} [−]	θ_{th} [°]	$\underline{\theta}_{th}$ [°]	$d\theta_{th}$ [°]	θ_{BW} [°]	$\underline{\theta}_{\mathrm{BW}}$ [°]	$d\theta_{\mathrm{BW}}$ [°]
A	0.00	-55.44	-52.67	2.76	-16.48	-11.78	4.70
B	0.22	-54.84	-52.31	2.53	-12.69	-7.75	4.93
C	0.30	-54.31	-51.93	2.38	-7.28	-2.18	5.10
D	0.33	-54.06	-51.77	2.29	0.00	2.43	2.43

slightly more axial than the theoretical one while the sonic line is not coincident with the segment JC′ leading to a non-constant pressure distribution. These two phenomena are described in detail in the following paragraph and in Section 5.3.

Spike below the Prandtl-Meyer expansion The portion of the spike, covered by the Prandtl-Meyer expansion, provides more thrust than the theoretical one due to the fillet shape which generates a non-pointwise expansion which delays the expansion. This phenomenon is investigated at Section 5.4.1.

Last part of the spike The thrust delivered by the last part of the spike is related to the flow alignment with the engine axis. Its magnitude increases as η_b^{bc} increases, because the spike becomes longer and longer, aligning more the flow with the engine axis. Except for the case A, in every simulation, $\Delta C_{F,\mathrm{slp}}$ is negative, and it decreases with increasing η_b^{bc}.

Base In agreement with Onofri [27], the base thrust contribution ranges from small drag to an almost neutral contribution in the over-expanded regime. The base thrust coefficient decreases as η_b^{bc} increases because most of the flow alignment happens on the spike. The theoretical base works better than the simulated one because in the theoretical case the flow leaves the spike more inclined towards the engine axis.

5.2.4. Improvement of the theory with simulation results

One of the issues of the theory introduced in Section 5.2.2 is the estimation of the flow direction at different engine sections. The major uncertainties are introduced at the throat section and at the spike end. From the simulation, the average flow direction over a generic j-th engine section can be calculated using the following formulas

$$\underline{\boldsymbol{\mathcal{F}}}_j = \frac{1}{\Delta t_{\mathrm{pp}}} \int_{t_a}^{t_b} \int_{S_j} \underline{\rho}(\mathbf{x},t)\, \underline{\mathbf{u}}(\mathbf{x},t) \left(\underline{\mathbf{u}}(\mathbf{x},t) \cdot \hat{\mathbf{n}} \right) dS\, dt \tag{29}$$

$$\underline{\mathbf{u}}_j = \frac{\underline{\boldsymbol{\mathcal{F}}}_j}{\underline{\dot{m}}} \tag{30}$$

$$\underline{\theta}_j = \operatorname{atan2}\left(\hat{\mathbf{r}} \cdot \underline{\mathbf{u}}_j, \hat{\mathbf{i}} \cdot \underline{\mathbf{u}}_j \right) \tag{31}$$

where $\hat{\mathbf{i}}$ and $\hat{\mathbf{r}}$ are the unit vectors pointing along the engine axis and along the radial direction respectively. t_a and t_b are the extreme values of the post-processing time interval: $\Delta t_{pp} = t_b - t_a$. They are equal to 60 ms and 70 ms respectively. The average velocity obtained with Equation (30), has the properties to conserve the average over the time of the momentum flux through the section S_j. Along the line BW, this average allows to neglect the flow which is external to the shear layer because due to low speed it does not contribute to the double integral in the Equation (29). Table 10 compares the theoretical flow direction with the ones calculated from the four simulations. The flow at the throat section is not perpendicular to the line JC′, but it is slightly tilted towards the axial direction. The maximum deviation is 2.76°. While the difference for the flow direction on the line BW is higher, and it reaches 5.10° in the case B. The flow exiting from the spike has a lower inclination than the theoretical one. This phenomenon is explained in Section 5.5.1.

Table 11
Individual thrust coefficient of every engine wall compared with the improved theoretical results.

Case		A	B	C	D
Converging nozzle	$\underline{C}_{F,\mathrm{cn}}$ [−]	−2.455	−2.440	−2.450	−2.444
	$C_{F,\mathrm{cn}}$ [−]	−2.478	−2.468	−2.459	−2.455
	$\Delta C_{F,\mathrm{cn}}$ [−]	0.023	0.029	0.009	0.011
	$\delta C_{F,\mathrm{cn}}$ [−]	1.919	2.409	0.752	0.915
Spike (Prandtl-Meyer expansion)	$\underline{C}_{F,\mathrm{spm}}$ [−]	0.473	0.474	0.498	0.498
	$C_{F,\mathrm{spm}}$ [−]	0.435	0.432	0.428	0.427
	$\Delta C_{F,\mathrm{spm}}$ [−]	0.038	0.042	0.070	0.072
	$\delta C_{F,\mathrm{spm}}$ [−]	3.168	3.497	5.840	5.965
Spike (last part)	$\underline{C}_{F,\mathrm{slp}}$ [−]	0.071	0.076	0.077	0.079
	$C_{F,\mathrm{slp}}$ [−]	0.091	0.104	0.114	0.114
	$\Delta C_{F,\mathrm{slp}}$ [−]	−0.019	−0.029	−0.037	−0.035
	$\delta C_{F,\mathrm{slp}}$ [−]	−1.595	−2.402	−3.089	−2.922
Base	$\underline{C}_{F,\mathrm{base}}$ [−]	0.024	0.008	−0.002	−0.010
	$C_{F,\mathrm{base}}$ [−]	0.025	0.011	0.001	0.001
	$\Delta C_{F,\mathrm{base}}$ [−]	−0.001	−0.003	−0.003	−0.011
	$\delta C_{F,\mathrm{base}}$ [−]	−0.104	−0.233	−0.238	−0.913

Table 11 shows the thrust coefficient obtained with the theory explained in Section 5.2.2 in which the theoretical angle has been substituted with the ones calculated from the simulations and shown in Table 10. Only the surfaces affected by the change of the two evaluated angles are shown in this table. The major discrepancy in the converging nozzle was the estimation of the flow inclination at the throat section. Indeed, using the averaged angle calculated from the simulations, it reduces $\Delta C_{F,\mathrm{cn}}$. The theoretical thrust coefficient of the converging nozzle is still lower. The issue is related to the pressure and velocity distribution along the line JC′. The uncertainty on the flow direction at the spike end has huge effect on the distribution of the thrust between the last part of the spike and the base. As shown in Table 10, the flow leaves the spike with a lower inclination than the spike slope, therefore this reduces the thrust that the base can recover because the flow must be diverted less to reach the axial direction. The update angles reduce the estimation error at the base of one order of magnitude.

5.3. Throat section

Fig. 12 shows pressure contours of the simulation with $\eta_b^{\mathrm{bc}} = 0.00$ near the throat section with the superimposed streamlines. The red dashed line is the constant pressure line corresponding to the sonic line while the red dashed one is the sonic line according to the isentropic nozzle theory: it goes from the point C′ to J. The dashed violet line is a shockwave which starts after the point C′. The locus of the point for which $M = 1.0$ is highlighted in blue in Figs. 13 to 16 which compare the contour plot of the Mach lines near the throat section with the ones predicted by a Prandtl-Meyer expansion. In every case, the sonic line is not straight, and it starts from the point J and ends in the middle of the line DC′, which means that in the previous analysis shown in Section 5.2, part of the supersonic expansion has been included into the calculation of $\underline{C}_{F,\mathrm{cn}}$. The combination of this phenomenon and the flow direction which is not perpendicular to the line JC′ but has a lower inclination (Table 10), leads to a higher thrust in the simulated convergent part with respect to the theoretical one. After the throat section JC′, the flow should become supersonic and a Prandtl-Meyer expansion, centre

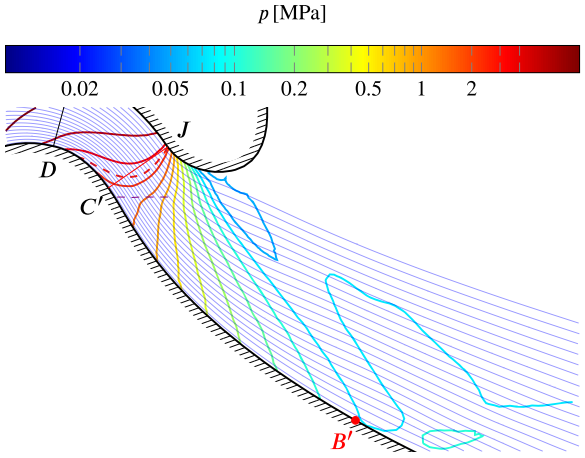

Fig. 12. Streamlines of modified DemoP1 simulation: case A, $\eta_b^{bc} = 0.00$, with the pressure contours superimposed. The point B′ highlights the theoretical position of the end of the Prandtl-Meyer expansion. The dashed red line corresponds to the isentropic pressure evaluate at the throat, while the dashed violet one is a weak oblique shockwave.

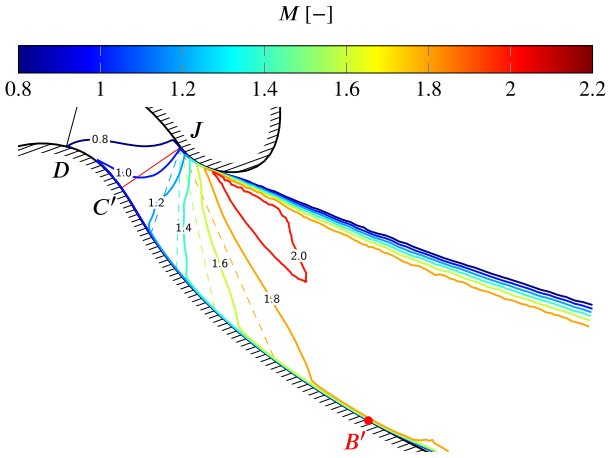

Fig. 13. Contours of Mach number of the simulation with $\eta_b^{bc} = 0.00$. The point B′ highlights the theoretical position of the end of the Prandtl-Meyer expansion.

in the point J, should drive the expansion, but due to the anticipated expansion near the lower wall, the flow becomes supersonic earlier, hence a non-centred expansion fan generated by the line DC′ drives the expansion near the wall. After the point C′, the flow near the wall is not guided by the centred expansion fan which originates from J because it occurs before its domain of influence, hence an oblique shockwave deviates the flow according to the wall. In Fig. 12, the shockwave is highlighted in violet, but it is too weak to be followed up to the shear layer. The Prandtl-Meyer theory predicts straight Mach lines exiting from the point J, but the Mach contours obtained from the simulations and shown in Figs. 13 to 16 highlight that these lines do not converge in J. The fillet delays the expansion generating Mach constant lines which are shifted ahead the ones predicted by Prandtl-Mayer theory. Far away from walls, the flow could be considered inviscid hence the constant Mach lines correspond also to constant pressure lines shown in Fig. 12. Therefore, the shifting of the lines corresponds to a higher pressure over the spike than the Prandtl-Mayer theory prediction. The pressure gradient, which is normal to the pressure constant lines, is not aligned with the streamlines because only a part of it accelerates the flow, the other component allows it to turn following the spike wall.

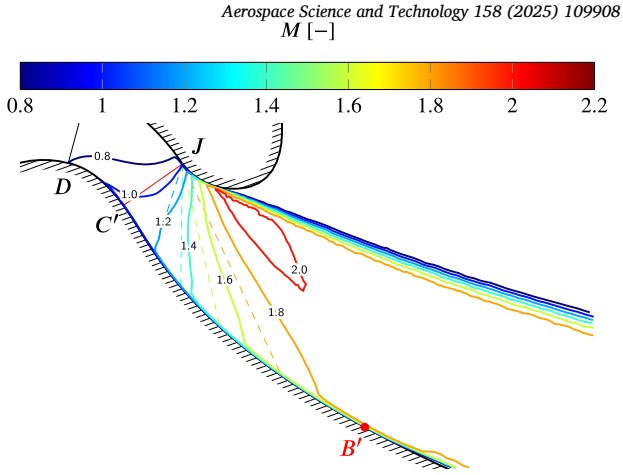

Fig. 14. Contours of Mach number of the simulation with $\eta_b^{bc} = 0.22$. The point B′ highlights the theoretical position of the end of the Prandtl-Meyer expansion.

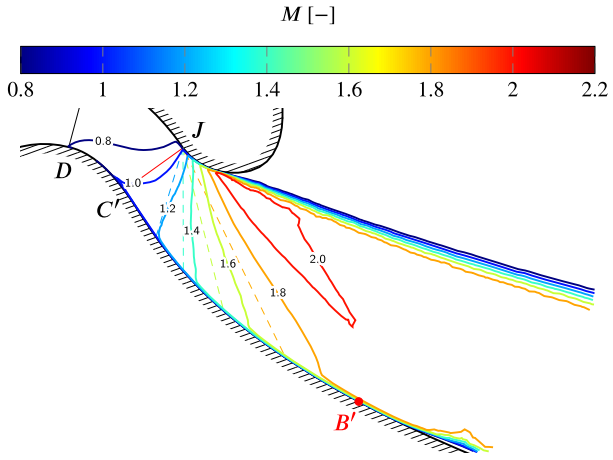

Fig. 15. Contours of Mach number of the simulation with $\eta_b^{bc} = 0.30$. The point B′ highlights the theoretical position of the end of the Prandtl-Meyer expansion.

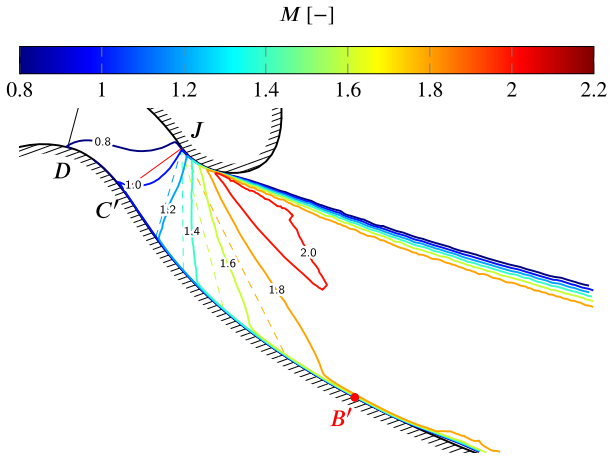

Fig. 16. Contours of Mach number of the simulation with $\eta_b^{bc} = 0.33$. The point B′ highlights the theoretical position of the end of the Prandtl-Meyer expansion.

5.4. Spike

5.4.1. Pressure distribution

Fig. 17 shows the relative pressure distribution along the spike and the base comparing them with the isentropic results. The theoretical pressure distribution has been obtained combining the Prandtl-Meyer

expansion with Angelino's theory [26]. s is a curvilinear coordinate that starts from the point F and follows the lower wall. Due to slightly different throat section locations, in every case, the Prandtl-Meyer expansion starts and ends at different values of s, but since they are very close to each other, only the average value has been displayed: $\hat{s}_{th}$ is the average curvilinear coordinate of the throat sections, and $\hat{s}_{\mathrm{B}'}$ is the average curvilinear coordinate of the Prandtl-Meyer expansion end. The coloured areas represent the local standard deviation of the pressure evaluated between 60 ms and 70 ms. The pressure distribution becomes less smooth at the throat section, and it is lower than the one predicted by the Prandtl-Meyer theory. This is the effect is related to the anticipated expansion at the throat section described in Section 5.3. The small pressure peaks are due to weak oblique compressive wave. After $\hat{s}_{th}$, the pressure decreases following an expansion which happens at higher pressure than the one predicted by Prandtl-Meyer theory. This is a consequence of the way the expansion occurs on the fillet, and it explains the higher pressure over the spike shown in Fig. 17. The direct consequence is a higher thrust delivered by the first portion of the spike (the one involved in the Prandlt-Meyer expansion zone) as shown in Tables 8, 9 and 11. At the same time, the constant pressure lines do not start in J creating a pressure imbalance over the fillet (Figs. 13 to 16). In the theoretical case, after the point J, the pressure is equal to the ambient one, therefore the fillet does not produce any thrust but in the actual case due to the lines lagging, it produces a negative thrust contribution. Close to the throat section, the Mach contour lines are not straight because they are influenced by the flow behaviour at the throat section. The theoretical Prandtl-Meyer expansion over the spike ends at $s_{\mathrm{B}'}$ but due to the pressure lag generated by the fillet, in the simulation, it ends in $\underline{s}'_{\mathrm{B}}$ with a pressure that is still slightly higher than the ambient one: this point is defined as the pressure local minimum after $s_{\mathrm{B}'}$; in Fig. 17, an average value $\underline{\hat{s}}_{\mathrm{B}'}$ has been displayed. Along the Prandtl-Meyer expansion, the flow is guided by expansion fan itself. It does not require the wall to change direction, while after the $\hat{s}_{\mathrm{B}'}$, the flow is guided by the wall therefore it can turn according to the wall only through shock waves and their reflection on the shear layer. After the $\hat{s}_{\mathrm{B}'}$, an oblique shockwave slightly increases the pressure leading to a flow detachment which is described in detail in Section 5.4.2. Subsequently, the flow is able to reattach back to the wall, then a second oblique shockwave further increases the pressure. In the last part of the spike, the pressure distribution is similar in the four cases because at the end of the Prandtl-Meyer expansion the flow changes direction of the same angle independently of the spike slope at the point B′. After the second oblique shockwave, the pressure increases linearly up to the spike end (s_{B}) where a final expansion drives the flow towards the base. For the longer spikes the higher pressure region is extended. In agreement with Table 11, the thrust detriment is related to the flow detachment which delays the high pressure region.

Considering only the pressure contribution, the infinitesimal thrust provided by an infinitesimal section of the spike is

$$dF = p_r(s)\, d\Psi \tag{32}$$

$$d\Psi = -2\pi r_w(s) \left[\hat{\mathbf{n}}_w(s) \cdot \hat{\mathbf{n}}_{ea}\right] ds \tag{33}$$

where $d\Psi$ is the infinitesimal variation of the projected area, $r_w(s)$ is the radius of the spike at the curvilinear coordinate s and $\hat{\mathbf{n}}_w(s)$ is the unit vector normal to the spike surface, pointing towards the flow. $\hat{\mathbf{n}}_w(s) \cdot \hat{\mathbf{n}}_{ea} = \cos\left(\frac{\pi}{2} - \delta_w(s)\right) = \sin\left(\delta_w(s)\right)$ where $\delta_w(s)$ is the spike slope. Fig. 18 shows the relative pressure distribution plotted with respect the cumulative area obtained integrating Equation (33):

$$\Psi(s) = \int_{s_{\mathrm{D}}}^{s} -2\pi r_w(\tau) \sin(\delta(\tau))\, d\tau \tag{34}$$

The point D has been chosen as left extreme of integration in Equation (34) because it has the same coordinate in every geometry. $\Psi(s)$ is the area of the spike projected into a plane normal to the engine axis, hence, Equation (34) can be rewritten as follows

$$\Psi(s) = \pi \left[r_{\mathrm{D}}^2 - r_w^2(s)\right] \tag{35}$$

$\hat{\Psi}_{th}$ and $\hat{\Psi}_{\mathrm{B}'}$ are average areas respectively related to $\hat{s}_{th}$ and $\hat{s}_{\mathrm{B}'}$. They have been obtained averaging the corresponding area of the four geometries. Ψ_{B} is the same in every geometry because the points D and B have the same radial coordinate in every simulation.[4] Fig. 18 shows that the four engines have the similar pressure distribution over the spike with respect the radial coordinate, while there are some differences at the throat section and at the base. The variation around the throat section is related to the different slope at the point C, which implies a different pressure distribution. Fig. 19 shows the cumulative thrust generated over the spike from the point D integrating Equation (32).

$$F_{\mathrm{sb}}(s) = \int_{s_{\mathrm{D}}}^{s} -2\pi r_w(\tau) \sin\left(\delta_w(\tau)\right) p_r(\tau)\, d\tau \tag{36}$$

The cumulative thrust shown in Fig. 19 quickly rises in the first part of the spike, while its derivative becomes almost zero close to the point B′, the end of the Prandtl-Meyer expansion. Then it rises again after the oblique shockwave located downstream the recirculating bubble over the spike. At the aerospike base, the cumulative thrusts display different behaviours. In the case A and B, it rises, while in the other cases, it decreases reaching the similar final value. According to Fig. 19, the four spikes provide almost the same amount of thrust, which means that the thrust gained by the geometry A with respect the geometry D at the base is lost in the region close to the throat section. The same argument is valid for the other geometries. According to Table 10, in the case A, the

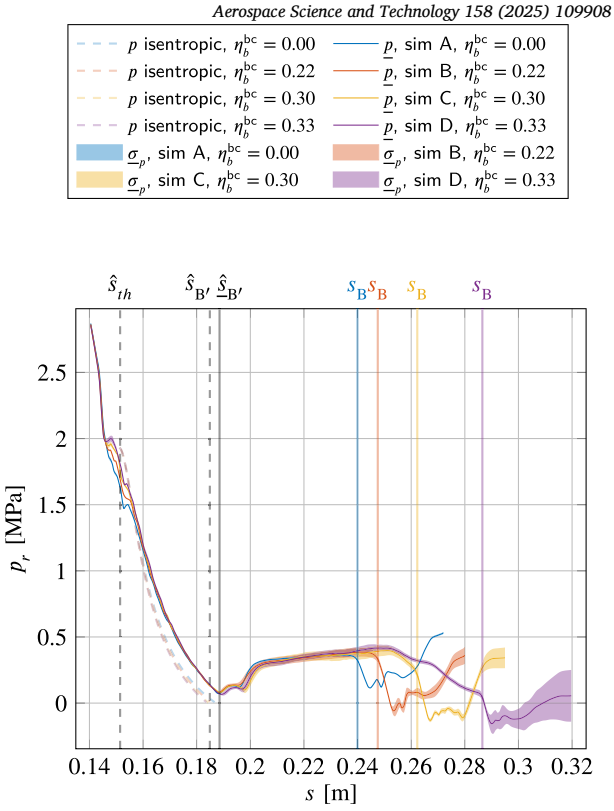

Fig. 17. Relative pressure distribution over the spike and the base compared with the isentropic results obtained combining the Angelino theory and the isentropic nozzle theory.

[4] Ψ is a cumulative area starting from the point D, hence $\Psi_{\mathrm{B}} \neq \pi r_{\mathrm{B}}^2$.

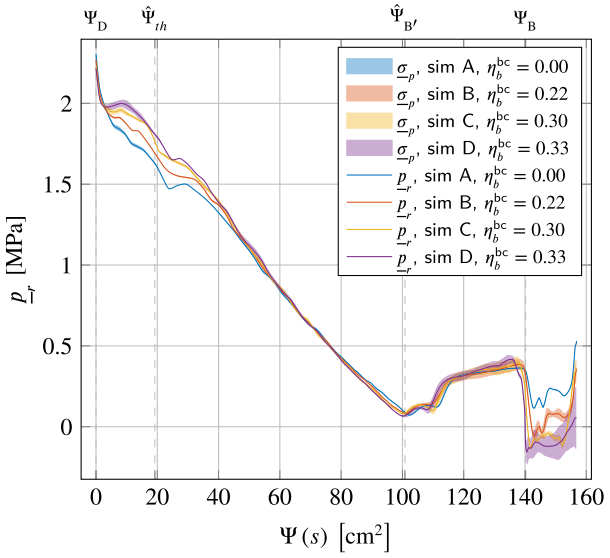

Fig. 18. Relative pressure distribution over the cumulative area.

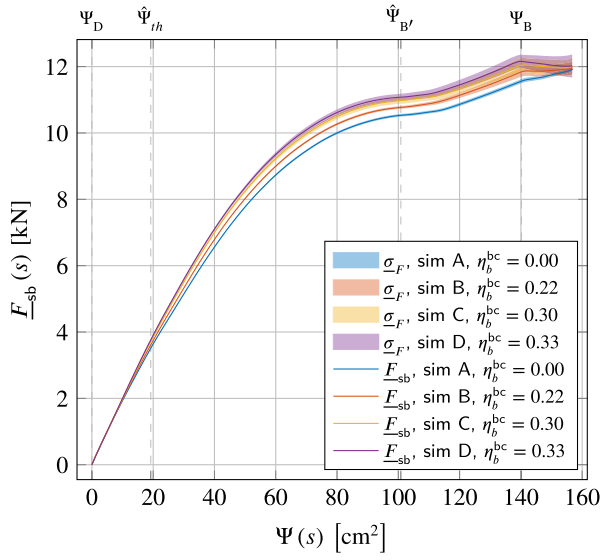

Fig. 19. Relative pressure distribution over the cumulative area.

flow has a lower inclination, hence a lower thrust is provided by the engine part before the throat section, and it is recovered by the base. While the opposite happens in the case D. Fig. 19 confirms that longer spike (case D) is able to generate higher thrust, but this gain is lost due to the base drag.

5.4.2. Flow separation over the spike

Fig. 20 shows the pressure contours close to the recirculating bubble in the middle of the spike with the superimposed streamlines. The violet dashed lines are the compression waves, while the violet dash-dotted lines are the expansion waves. Below this plot there is the relative pressure distribution and τ_w along the spike with respect to the engine axis: the origin of the reference frame is shown in Fig. 5. τ_w is defined as the projection of the wall shear stress along the wall tangent direction

$$\tau_w = \hat{\mathbf{n}}_w^T \boldsymbol{\tau}_w \cdot \hat{\mathbf{t}}_w \tag{37}$$

where $\hat{\mathbf{n}}_w$, $\hat{\mathbf{t}}_w$ are respectively the unit vector normal and tangent to the spike, while $\boldsymbol{\tau}_w$ is the shear stress tensor evaluated at the wall. The information shown is extracted at one time instance, hence they are not averaged in time. As it is highlighted in Fig. 20, after the Prandtl-Meyer

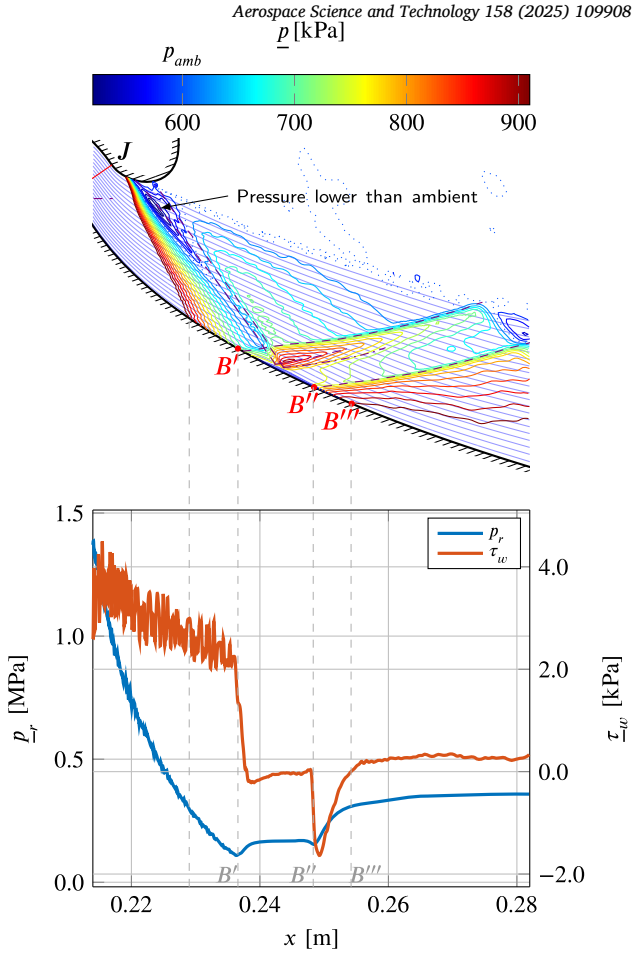

Fig. 20. Pressure contours around the recirculating bubble in the middle of the spike with superimposed the streamlines. The dotted blue line represents the ambient pressure. The dashed violet lines are the compression waves while the dash dotted are the expansion waves. The second plot shows the relative pressure distribution along the wall with the superimposed wall shear stress projected along the wall: on x-axis there is the engine axial coordinate. These values are not averaged in time.

expansion there are two oblique shockwaves. The first one starts from the fillet because the flow close to it continues to expand at pressures lower than the ambient one, therefore an oblique shockwave recompresses it. The second shockwave is related to the one generated after the point C′. As it has been shown in Section 5.3, a shockwave spreads after the point C′ towards the region below the fillet. Due to the weakness of this recompression, it is hard to identify it, but it should reach the last expansion line of Prandtl-Meyer expansion. This shockwave leads to a recompression which is followed by an expansion that reduces the pressure at values lower than the ambient one, producing the region highlighted in dark blue in Fig. 20: the dotted blue line corresponds to the ambient pressure. Subsequently, this low pressure flow is recompressed by the first and the second shockwaves. These two shockwaves reach the boundary layer after the point B′ generating a Shock Wave Boundary Layer Interaction (SWBLI) [40–42] which can be classified as strong interaction because the flow separates from the wall generating a recirculating bubble. As indicated by the wall shear stress in Fig. 20, the adverse pressure gradient generates from the impinging shockwaves is sensed upstream through the subsonic region close to the wall producing a recirculating bubble which starts slightly after the point B′ and ends in B″: the bubble covers the region of the spike where τ_w is negative. Slightly after the point B′, a recompression wave, shown with a dashed violet line in Fig. 20, deviates the flow around the bubble. An expansion fan, highlighted with violet dash-dotted lines, expands the flow beyond

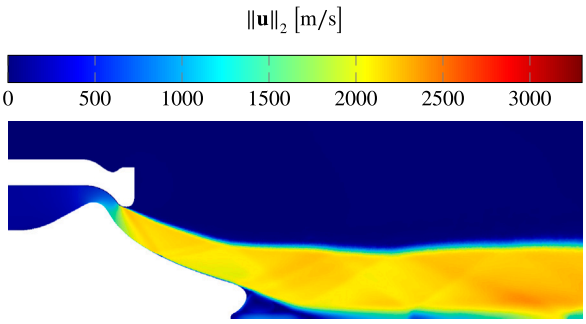

Fig. 21. Velocity magnitude field of modified DemoP1 simulation: case A, $\eta_b^{bc} = 0.00$.

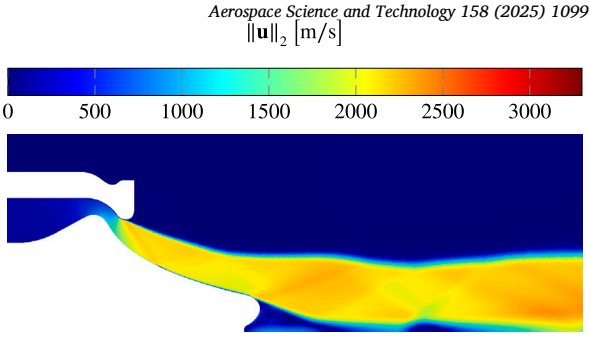

Fig. 22. Velocity magnitude field of modified DemoP1 simulation: case B, $\eta_b^{bc} = 0.22$.

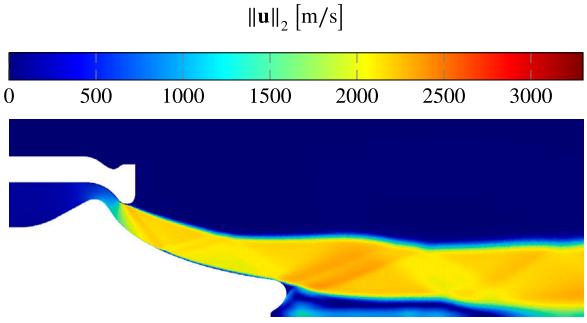

Fig. 23. Velocity magnitude field of modified DemoP1 simulation: case C, $\eta_b^{bc} = 0.30$.

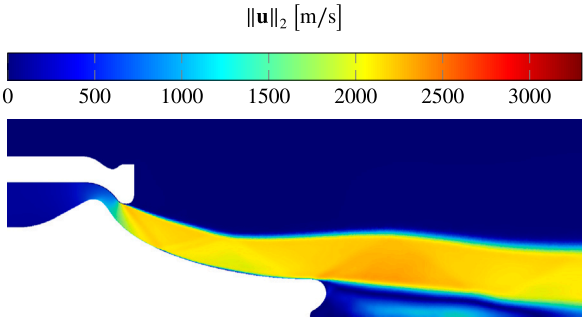

Fig. 24. Velocity magnitude field of modified DemoP1 simulation: case D, $\eta_b^{bc} = 0.33$.

the recirculating bubble and then a compression wave starting from B″ aligns the flow with the spike wall. According to Dèlerey and Dussauge in [43], the pressure rises at the flow separation, then it rises again at the reattachment point. This flow separation pattern is called Restricted Shock Separation (RSS) and is a canonical shock/boundary layer interaction characterized by a small separation region [44]. It has already been investigated on a conical aerospike by He in [45]. This type of separation occurs also in the bell-shaped nozzles of engines like the Vulcain [46], and the Space Shuttle Main Engine (SSME) [46]. As it can be noticed in Fig. 17, the recirculating bubble retards the oblique shockwave position leading to a thrust loss because the higher pressure region is shifted to the end of the spike. The amount of thrust loss can not be easily evaluated because the pressure distribution shown in Fig. 17 can not be simply shifted towards the left. A second recirculating bubble is located between B″ and B‴ according to the negative value of the wall shear stress shown in Fig. 20.

5.5. Base

5.5.1. Thrust recovered by the base

The results shown in Table 9, confirm that increasing η_b^{bc}, the theoretical base contribution decreases reaching 0 N for $\eta_b^{bc} = 0.33$; this happens because in over-expansion condition the base can recover only the thrust related to the alignment of the flow with the engine axis, because the flow has already reached the ambient pressure over the spike, meaning that the flow can not be further expanded. When $\eta_b^{bc} = 0.33$, the flow leaves the spike almost in the axial direction, hence the base should not recover any thrust. In the simulation results, the base thrust contribution decreases as η_b^{bc} decreases, but in the geometry D, the thrust contribution instead of being zero, it becomes negative leading to a thrust loss. This phenomenon can be explained looking at Figs. 21 to 24 that show the velocity magnitude field in the four simulations. As η_b^{bc} increases, the spike axial length increases and the flow leaves the spike with a lower inclination with respect to the axial direction. This leads to an earlier flow detachment from the base wall, visible in Figs. 23 and 24, which creates a low pressure region that is visible in Figs. 17 and 18. The recirculating bubble has almost the same size in the geometries A and B, while it grows in C and D.

In these images, it is possible to recognize the flow topology of an aerospike. In every figure, the Prandlt-Meyer expansion is visible near the throat; this expansion ends on the spike, and it is followed by a recompression which turns the flow along the last part of the spike. The recompression is reflected by the shear layer but only in case D reaches again the spike. In Figs. 21 to 23, another expansion turns the flow towards the base and a subsequently trailing shock deviates it in the axial direction. The trailing shock is located at the end of the recirculating bubble, hence in the case with $\eta_b^{bc} = 0.33$, the flow is turned into the axial direction faraway from the base.

Figs. 25 to 28 show the streamlines created on average velocity field. In Figs. 25 and 26, the recirculating bubble is small and has a triangular

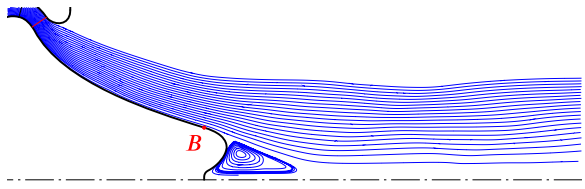

Fig. 25. Streamlines of modified DemoP1 spike simulation: case A, $\eta_b^{bc} = 0.00$.

shape, while in Figs. 27 and 28, it is elongated leading to a more unsteady flow and thrust oscillations. These images show why increasing η_b^{bc} leads to an increment of the thrust losses with respect the isentropic nozzle theory. To achieve the highest thrust, the flow should leave the engine in the axial direction. In the case A, the streamlines leave the spike with an inclination towards the engine axis but in front of the base they become almost aligned with it. While in the B, C and D cases, they leave the spike more horizontally but after the point B, the flow turns toward the base.

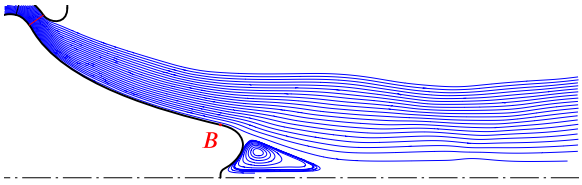

Fig. 26. Streamlines of modified DemoP1 spike simulation: case A, $\eta_b^{bc} = 0.22$.

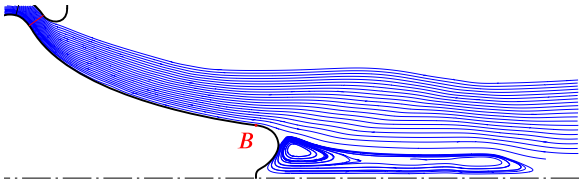

Fig. 27. Streamlines of modified DemoP1 spike simulation: case A, $\eta_b^{bc} = 0.30$.

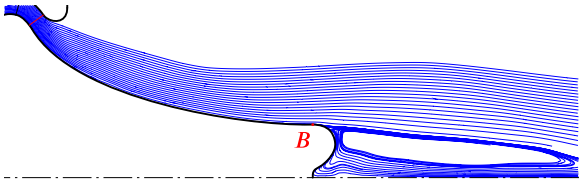

Fig. 28. Streamlines of modified DemoP1 spike simulation: case A, $\eta_b^{bc} = 0.33$.

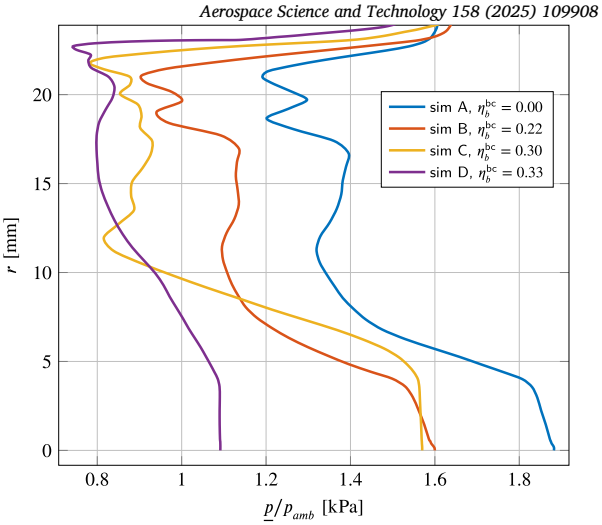

Fig. 29. Ratio between pressure at the aerospike base and the ambient one at different radial coordinate.

5.5.2. *Base pressure distribution*

Fig. 29 highlights the relative pressure distribution at the base. From this plot, it is clear that the pressure at the base decreases with increasing η_b^{bc}. This effect is related to the flow inclination at the end of the spike. Increasing η_b^{bc}, the flow leaves the aerospike more horizontally, hence it detaches earlier from the base creating the low pressure region. Close to the engine axis, the pressure rises reaching higher values than the ambient one. According to Bannik [47], the pressure at the nozzle base of the aerospike is influenced by the ambient pressure as long as the compression waves impinge on the inner shear layer, which starts approximatively from the point B and divides the high speed flow from the recirculating bubble in front of the base. This regime is called *open wake* [27]. The radial pressure distribution over the base, shown in Fig. 29, is in agreement with the results show by Chutkey in [48, Fig. 13a]. In that case a little higher nozzle pressure ratio ($NPR = 10$) has been considered, but the pressure distribution presents the same trend: near the lip, the pressure decreases and then grows back near the engine axis reaching higher values than the ambient pressure. The pressure drop ($\frac{p}{p_{amb}} < 1$) between $10\,\text{mm} \leq r \leq 20\,\text{mm}$ is more relevant than the pressure increment ($\frac{p}{p_{amb}} > 1$) near the engine axis, hence the contribution of this region determines the overall thrust provided by the base.

5.5.3. *Recirculating bubble length*

The estimation of the recirculating bubble length could be done using the results introduced by Chang in [49] and by Herrin in [50]. These two studies determine that for a Mach number higher than 2, in the supersonic backward-facing step, the recirculating bubble has a length that is independent of the Mach number, and it can be estimated as follows

$$l_{rb} \approx 2.65 r_B \tag{38}$$

In [51], Nasuti has extended this model to the aerospike introducing the dependency from the spike slope achieving the following correlation

$$l_{rb} \approx \left(2.65 - 0.00144\delta_B^2\right) r_B \tag{39}$$

where δ_B is the spike inclination at the point B. The Mach number at the spike end, can be estimated solving Equation (23) at point B. The obtained Mach number grows with η_b^{bc}, from 2.43 up to 2.74, therefore the previous theory can be applied. Fig. 30 compares the average bubble length l_{rb} calculated from the simulations with the one estimated using Equations (38) and (39). For case A and B, the model proposed by Nasuti, is quite close to the length obtained by the simulations, while for the case C and D, both models underpredicts the length of the recirculating bubble. This discrepancy can be justified in three ways. Firstly, the two models have been obtained from geometries that have a sharp edge between the spike and the base. Secondly, the Nasuti's model has been obtained from aerospike geometries where the lowest slope at the point B is 10°, hence the geometries C and D are out of the validity range. This model is a modification of the Chang's one, therefore for $\delta_B = 0.0$, it outputs the same result, but the Chang's model has been obtained from the backward facing step which supposes a uniform inlet flow which is just true for the aerospike as first approximation. Finally, as shown by Table 10, the flow inclination is lower than the spike slope by some degrees. For example, in the case D, the flow is leaving the spike pointing far away from the engine axis instead of being parallel to it, therefore, the correlation found by Nasuti can be improved using the actual flow inclination instead of the spike slope. Despite that, more data are needed to obtain an accurate description of l_{rb} as function of the flow direction at the spike end. Fig. 30 also shows the minimum and the maximum recirculating bubble length and, in agreement with the pressure distribution standard deviation shown in Fig. 17, the difference between the maximum and minimum recirculating bubble length increases decreasing δ_B.

5.6. *Thrust oscillations*

Fig. 8 and the thrust standard deviation, reported in Table 3, highlight the presence of thrust oscillations that increases in amplitude as η_b^{bc} increases. This phenomenon is highlighted by Fig. 31 which shows the thrust variation during the simulations. Not only the amplitude increases but also the oscillation frequency grows. This thrust oscillation also affects the specific impulse as shown in Fig. 9. Fig. 17 shows the pressure standard deviation calculated in the post-processing time interval ($60\,\text{ms} \leq t \leq 70\,\text{ms}$) which highlights the location of the thrust oscillation source. The pressure standard deviation increases slightly near the throat section and then decreases during the Prandlt-Meyer expansion. Then it increases again at the recirculating bubble over the spike and after the oblique shockwave. During the expansion which starts at the end of the spike, it is low and increases at the base. Hence, the source

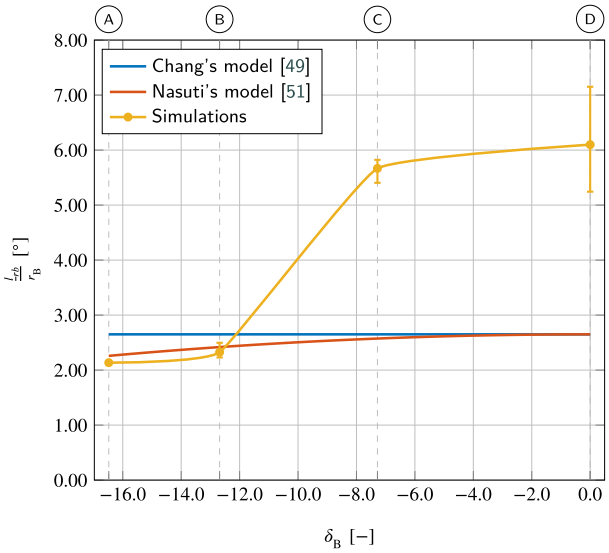

Fig. 30. Dimensionless average length of the recirculating bubble in front of the aerospike base compared with the length estimated by the Chang's model [49] and the Nasuti's one [51]. The error bars represent the minimum and maximum recirculating bubble length.

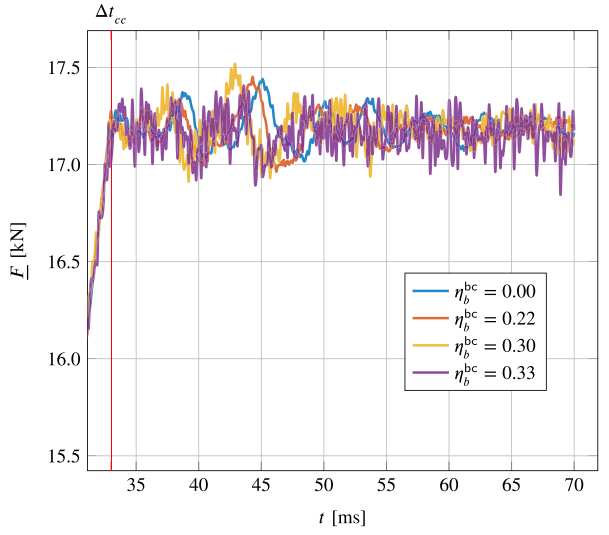

Fig. 31. Thrust variation in time at different η_b^{bc} values: Δt_{cc} is the time instance at which the inlet transient ends.

of the oscillations is related to flow separation in the middle and at the end of the spike. Increasing η_b^{bc} the flow leaves the spike with a lower inclination that leads to a larger recirculation region in front of the base which increases the thrust oscillation.

Fig. 31 confirms that between 60 ms and 70 ms, the solution reaches a quasi-steady condition.

5.7. Spike weight estimation

The engine mass can be broken down in four parts listed in the following equation

$$m_{eng} = m_{sb}\left(\eta_b^{bc}\right) + m_{cc} + m_{cn} + m_{ew} \tag{40}$$

where m_{cc} is the mass of the combustion chamber, m_{cn} is the converging nozzle mass, m_{ew} is the one of the external wall and $m_{sb}\left(\eta_b^{bc}\right)$ is the sum of the spike and base mass. It has been assumed that the latter is the only part of the engine which is influenced by η_b^{bc}. $m_{cc} + m_{cn} + m_{ew}$

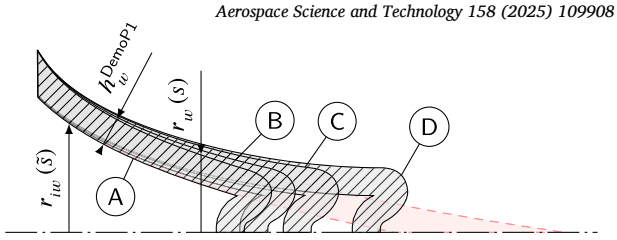

Fig. 32. Four simulated spike shapes and the equivalent plug nozzle one coloured red.

has been calculated from the Computer-Aided Design (CAD) drawing of DemoP1. DemoP1 has a constant thickness wall along the spike and the base, therefore, the engines, considered in this study, have been designed with a constant thickness wall that is equal to the DemoP1 wall thickness: $h_w^{DemoP1} = 10\,\text{mm}$. The spike and base mass have been evaluated using Equation (42)

$$V_{sb}\left(h_w^{DemoP1}\right) = \pi\left(\int_{s_{th}}^{s_A} r_w^2(\tau)\,d\tau - \int_{\tilde{s}_{th}}^{\tilde{s}_A} r_{iw}^2(\tau, h_w^{DemoP1})\,d\tau\right) \tag{41}$$

$$m_{sb} = \rho_w^{eq} V_{sb}\left(h_w^{DemoP1}\right) \tag{42}$$

where $r_w(s)$ and $r_{iw}(\tilde{s})$ are respectively the radius coordinate of the wall surface in contact with the hot gases and the internal one. The curve $r_{iw}(\tilde{s})$ has been obtained offsetting of a distance h_w^{DemoP1}, the line $r_w(s)$ along its surface local normal direction. s is the curvilinear coordinate that starts from the point F and follows the lower wall, s_{th} and s_A are respectively the curvilinear coordinate of the throat section and of the end points of the base (point A). The coordinate $\tilde{s}$ is defined in the same way of s but on the offset wall line. $\tilde{s}_{th}$ and $\tilde{s}_A$ are the corresponding points to s_{th} and s_A on the offset line. ρ_w^{eq} is the equivalent wall density which should take in account the mass of the axial pipe which brings the cold fuel to the aerospike base and the presence of the cooling channel inside the wall. The first increases the ρ_w^{eq} value, while the latter reduces it. The equivalent wall density could be calculated from the DemoP1 geometry for which m_{sb} is known from CAD drawing:

$$\rho_w^{eq} = \frac{m_{sb}^{DemoP1}}{V_{sb}\left(h_w^{DemoP1}\right)} = 1.00 \times 10^4\,\text{kg/m}^3 \tag{43}$$

The original DemoP1 has been manufactured using GRCop-42 which is a copper alloy developed by NASA [23] to have a high thermal conductivity while retaining good mechanical properties. This material has a maximum theoretical density of $8.89 \times 10^3\,\text{kg/m}^3$ [52,53]. The equivalent density ρ_w^{eq} is a bit higher than it.

$m_{sb}\left(\eta_b^{bc}\right)$ can be divided by the mass of an equivalent plug nozzle that has the same exit section area and expansion ratio $\frac{\mathcal{A}_e}{\mathcal{A}_{th}}$. The plug shape can be obtained using the Angelino's method described in [26] imposing $\eta_b^{bc} = 0.00$ and $p_{cut} = 0.00$. Also in this case, the internal wall has been designed offsetting the spike and base shape of h_w^{DemoP1}.

$$\bar{m} = \frac{m_{sb}}{m_{plug}} \tag{44}$$

The four spikes designed are shown in Fig. 32 together with the equivalent plug nozzle highlighted in red. Fig. 33 shows the dimensionless mass with respect to η_b^{bc}. Increasing η_b^{bc}, mass ratio increases and already from the case C, the spike and base are heavier than the equivalent plug nozzle. Fig. 34 shows the thrust-to-mass ratio which decreases increasing η_b^{bc}. From these two figures, it is clear that using shorter spikes leads to an advantage in terms of thrust-to-mass ratio and a lower pressure drop along the cooling channels because they are shorter.

6. Fillet effect

The ideal aerospike has a sharp edge in the upper part of the throat section to force the Prandtl-Meyer expansion to be centred in the point J. Due to the additive manufacturing limitation, it is not possible to obtain

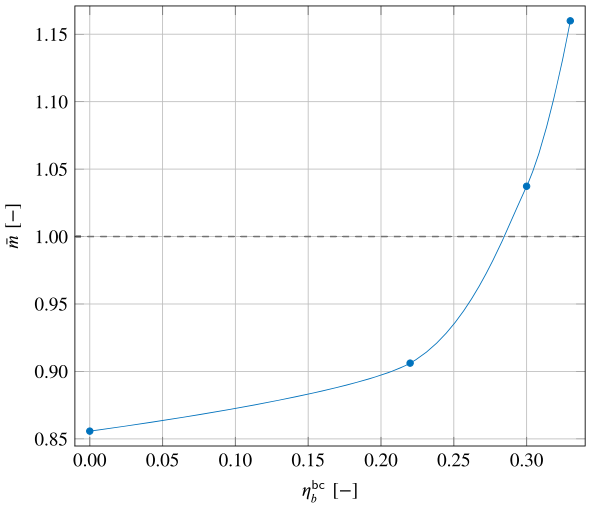

Fig. 33. Ratio between the mass of the spike and base of the simulated cases and the mass of the plug nozzle designed with the same exit section radius.

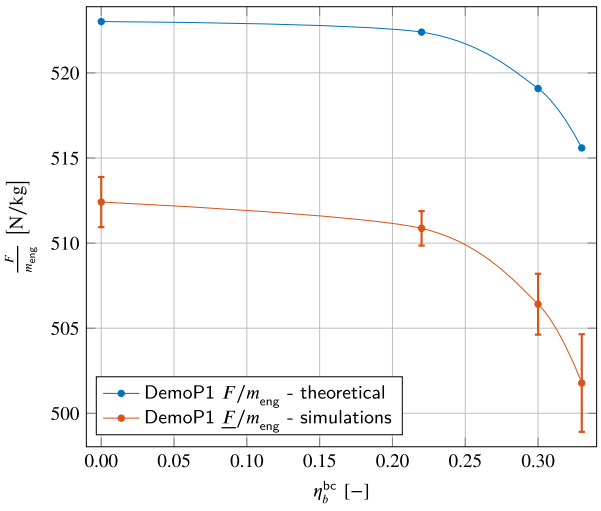

Fig. 34. Ratio between the thrust and the engine mass. The error bars are related to the thrust oscillations.

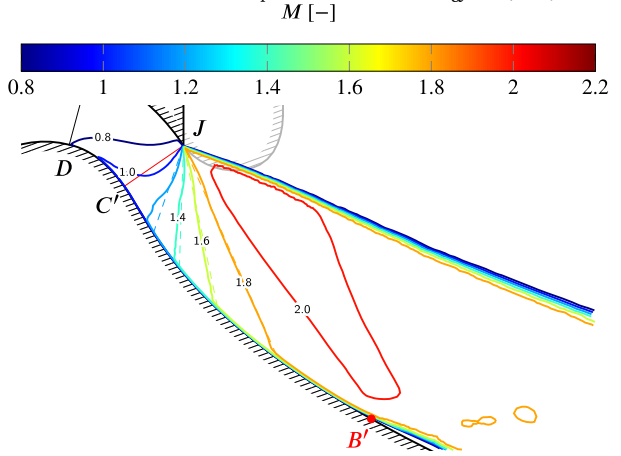

Fig. 35. Contour of Mach number of the simulation with $\eta_b^{bc} = 0.00$ and a sharp edge at the point J. The point B′ highlights the theoretical position of the end of the Prandtl-Meyer expansion. The grey wall represents the geometry with the fillet.

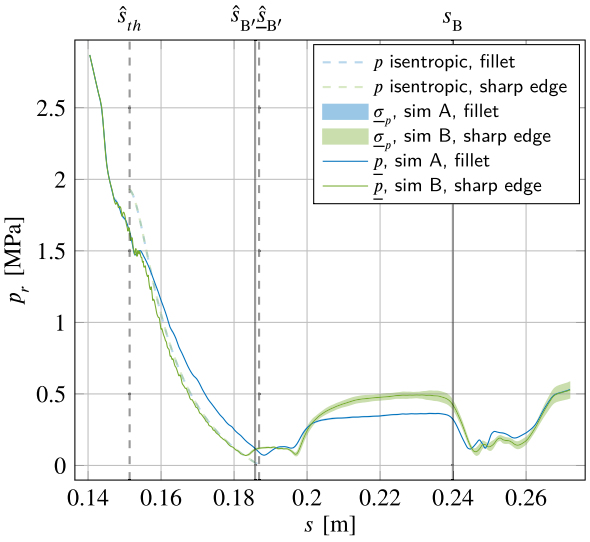

Fig. 36. Relative pressure distribution over the spike in the case with and without the sharp edge at the point J.

a sharp edges, therefore a fillet has been added to connect the point J with L. The sharp edge is also discarded because the tip cannot be cooled enough to keep a temperature for which the material still has good mechanical properties. Nevertheless, it is interesting to analyze the effect of the fillet on the expansion, therefore the geometry A has been modified with a sharp edge at the point J: the vertical wall has been translated towards the left. Fig. 35 compares the Mach number contour obtained from the simulation with the theoretical one. Close to the throat section there is a similar pattern shown in Fig. 13 in which the lines at constant Mach number are curved. Moving far away from the throat section, the lines are almost overlapped with the theoretical one confirming that the fillet delays the expansion.

Fig. 36 compares the relative pressure distribution along the spike between the geometry with and without the sharp edge at the point J. Also, this plot confirms that the fillet delays the expansion over the initial part of the spike. In the case with the sharp edge, the expansion follows the pressure distribution predicted by the Prandtl-Meyer theory, only close to the throat section the pressure is lower due to the phenomenon explained in Section 5.3. The expansion stops a pressure higher than the ambient one because the flow detaches from the spike as in the other cases, but differently from them, the recirculating bubble is large. Then, at almost the same coordinate, an oblique shock recompresses the flow, increasing the pressure more than the case with the fillet. The pressure distribution at the base is similar in both cases.

Fig. 37 shows the pressure contours of the geometry with the sharp edge averaging the pressure distribution between 60 ms and 70 ms. Also in the geometry with the sharp edge, the shockwave generated immediately after the throat section leads to an over-expansion at the end of the Prandtl-Meyer expansion. The low pressure region is coloured in dark blue in Fig. 37, and it is bounded by a dotted line which corresponds to the ambient pressure. This low pressure region is followed by shockwaves that recompress the flow up to the ambient pressure, but differently from the ones shown in Fig. 20, they only start from the shear layer. Also in this case, the shockwave reaches the boundary layer over the spike inducing the formation of a recirculating bubble. An oblique shock starts before the point B′ to deviate the flow around the recirculating bubble, and it is followed by a smaller expansion fan over the bubble.

Table 12 summarized the thrust coefficients per surface. The fillet generates a drag because the expansion is not pointwise, but it is distributed from the point J towards the point K, which is the lowest point along the JL line. At the same time, it has a positive effect because it increases the thrust of the first part of the spike because the expansion

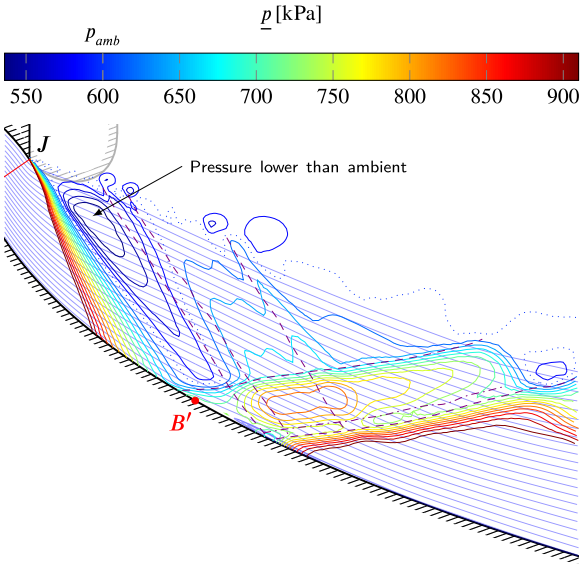

Fig. 37. Pressure contours around the recirculating bubble in the middle of the spike with superimposed the streamlines. The dashed violet lines are the compression waves while the dash dotted are the expansion waves.

Table 12
Individual thrust coefficient of every engine wall compared with the theoretical results and the geometry with and without the fillet ($\eta_b^{bc} = 0.00$).

Surface	Theoretical	Fillet	Sharp edge
$\underline{C}_{F,\text{inlet}}$ [−]	3.127	3.122	3.122
$\underline{C}_{F,\text{cc}}$ [−]	0.000	0.000	0.000
$\underline{C}_{F,\text{cn}}$ [−]	−2.504	−2.455	−2.471
$\underline{C}_{F,\text{fillet}}$ [−]	0.000	−0.059	0.000
$\underline{C}_{F,\text{spm}}$ [−]	0.461	0.473	0.418
$\underline{C}_{F,\text{slp}}$ [−]	0.067	0.071	0.088
$\underline{C}_{F,\text{base}}$ [−]	0.049	0.024	0.022
$\underline{C}_F$ [−]	1.200	1.175	1.177

delay shifts the pressure distribution downstream. In the last part of the spike, the pressure distribution is higher in the case with the sharp edge because the flow undergoes a greater deviation. Hence, the higher pressure distribution and the lower flow inclination at the spike end explains why the thrust coefficient calculated on the last part of the spike is higher in the case with the sharp edge, while the base generates slightly less thrust because the flow leaves the spike with a lower inclination.

7. Conclusion

In this work, four geometries have been generated using Angelino's method and then cut to achieve the same base radius. The main results of this analysis are the correlation between the thrust losses and the spike end slope. Increasing the spike slope at its end leads to a smaller recirculating bubble in front of the aerospike base because the flow is more directed toward the engine axis. This also slightly increases the thrust and reduces the thrust oscillation because the pressure drop at the base is smaller. A longer spike also implies longer cooling channels, i.e. higher pressure drops along the cooling system, heavier engines and lower thrust-to-mass ratio, hence at constant base radius the spike length should be reduced to improve the engine performance.

The sonic line shape at the throat section leads to an anticipated flow transition from subsonic to supersonic flow. This generates a shockwave immediately after the throat section to align the flow with the wall. This shockwave generates an over-expansion after the end of the main expansion fan generated from the upper wall. Then the flow is recompressed by oblique shockwaves which reach the boundary layer developed on the spike wall inducing a flow separation. The recirculating bubble generated from the shockwave boundary layer interaction delays the pressure increment leading to thrust losses.

The flow viscosity is responsible for the boundary layer development at the throat, reducing the mass flow rate, which directly reduces the thrust.

Each tested geometry has the same radial pressure distribution over the spike, the major difference is located at the throat section and at the aerospike base. In every geometry, the thrust recovered at the base is lost near the throat section or vice versa.

The models to estimate the recirculating bubble length in front of the aerospike base, that could be found in literature, give results that are close to the simulation for the cases A and B, while for the case C and D, they underpredict the recirculating bubble length.

The fillet has the effect to delay the expansion. This phenomenon leads to an opposite effect on the overall thrust. Differently from the sharp edge geometry, the expansion fan is not centred, hence the pressure distribution over the fillet generates a negative thrust. The delay on the expansion directly affects the pressure distribution over the spike which results to be higher than the theoretical one. Hence, the initial part of the spike delivers more thrust than the theoretical one. The overall effect of the fillet is to slightly reduce the thrust.

CRediT authorship contribution statement

Luca Fadigati: Writing – original draft, Validation, Software, Resources, Methodology, Investigation, Formal analysis, Conceptualization. **Ernesto Sozio:** Writing – review & editing, Supervision, Methodology, Investigation, Formal analysis, Data curation. **Federico Rossi:** Writing – review & editing, Supervision, Conceptualization. **Nabil Souhair:** Writing – review & editing, Supervision, Software, Methodology, Conceptualization. **Fabrizio Ponti:** Writing – review & editing, Visualization, Validation, Supervision, Formal analysis, Data curation, Conceptualization.

Declaration of competing interest

The authors declare that they have no known competing financial interests or personal relationships that could have appeared to influence the work reported in this paper.

Data availability

The data that has been used is confidential.

References

[1] G.P. Sutton, O. Biblarz, Rocket Propulsion Elements, ninth ed., Wiley, 2017.
[2] Philip G. Hill, Carl R. Peterson, Mechanics and Thermodynamics of Propulsion, second ed., Pearson, 1992.
[3] E. Schwarzer-Fischer, J. Abel, J. Sieder-Katzmann, M. Propst, C. Bach, U. Scheithauer, A. Michaelis, Study on CerAMfacturing of Novel Alumina Aerospike Nozzles by Lithography-Based Ceramic Vat Photopolymerization (CerAM VPP), Materials, vol. 15, 2022, p. 3279, https://www.mdpi.com/1996-1944/15/9/3279, number: 9, Publisher: Multidisciplinary Digital Publishing Institute.
[4] Pangea Aerospace, https://pangeaaerospace.com/, 2023.
[5] F. Rossi, G. Esnault, Z. Sápi, N. Palumbo, A. Argemi, R. Bergström, Research activities in the development of DemoP1: a LOX/LNG aerospike engine demonstrator, https://www.researchgate.net/publication/350800053_Research_Activities_in_the_Development_of_DemoP1_A_LOXLNG_Aerospike_Engine_Demonstrator, 2021.
[6] F. Rossi, Z. Sápi, N. Palumbo, A. Demediuk, M. Ampudia, Manufacturing and hot-fire test campaign of the DemoP1 aerospike engine demonstrator, Estroil, Portugal, https://www.researchgate.net/publication/360568621_Manufacturing_and_Hot-Fire_Test_Campaign_of_the_DemoP1_Aerospike_Engine_Demonstrator, 2022.
[7] Aenium Engineering - High Performance Additive Manufacturing, https://aenium.es/, 2023.
[8] Flight of the aerospike, Met. Powder Rep. 76 (2021) 12–15, https://doi.org/10.1016/S0026-0657(21)00296-4, https://www.sciencedirect.com/science/article/pii/S0026065721002964.

[9] H. Tian, Z. Guo, Z. Hao, L. Hedong, C. Li, Numerical and experimental investigation of throttleable hybrid rocket motor with aerospike nozzle, Aerosp. Sci. Technol. 106 (2020) 105983, https://doi.org/10.1016/j.ast.2020.105983, https://www.sciencedirect.com/science/article/pii/S1270963820306659.

[10] R. Li, J. Xu, H. Lv, D. Lv, J. Song, Numerical investigations of the nozzle performance for a rocket-based rotating detonation engine with film cooling, Aerosp. Sci. Technol. 136 (2023) 108221, https://doi.org/10.1016/j.ast.2023.108221, https://www.sciencedirect.com/science/article/pii/S1270963823001189.

[11] Y. Huang, H. Xia, X. Chen, Z. Luan, Y. You, Shock dynamics and expansion characteristics of an aerospike nozzle and its interaction with the rotating detonation combustor, Aerosp. Sci. Technol. 117 (2021) 106969, https://doi.org/10.1016/j.ast.2021.106969, https://www.sciencedirect.com/science/article/pii/S127096382100479X.

[12] Y. Zhu, K. Wang, Z. Wang, M. Zhao, Z. Jiao, Y. Wang, W. Fan, Study on the performance of a rotating detonation chamber with different aerospike nozzles, Aerosp. Sci. Technol. 107 (2020) 106338, https://doi.org/10.1016/j.ast.2020.106338, https://www.sciencedirect.com/science/article/pii/S1270963820310208.

[13] J.Z. Ma, W. Bao, J.-p. Wang, Experimental research of the performance and pressure gain in continuous detonation engines with aerospike nozzles, Aerosp. Sci. Technol. 140 (2023) 108464, https://doi.org/10.1016/j.ast.2023.108464, https://www.sciencedirect.com/science/article/pii/S1270963823003619.

[14] D. Shen, J.Z. Ma, Z. Sheng, G. Rong, K. Wu, Y. Zhang, J. Wang, Spinning pulsed detonation in rotating detonation engine, Aerosp. Sci. Technol. 126 (2022) 107661, https://doi.org/10.1016/j.ast.2022.107661, https://www.sciencedirect.com/science/article/pii/S1270963822003352.

[15] X.-Y. Liu, M. Cheng, Y.-Z. Zhang, J.-P. Wang, Design and optimization of aerospike nozzle for rotating detonation engine, Aerosp. Sci. Technol. 120 (2022) 107300, https://doi.org/10.1016/j.ast.2021.107300, https://www.sciencedirect.com/science/article/pii/S1270963821008105.

[16] C.-H. Wang, Y. Liu, L.-Z. Qin, Aerospike nozzle contour design and its performance validation, Acta Astronaut. 64 (2009) 1264–1275, https://doi.org/10.1016/j.actaastro.2008.01.045, https://www.sciencedirect.com/science/article/pii/S0094576509000204.

[17] M. Geron, R. Paciorri, F. Nasuti, F. Sabetta, Flowfield analysis of a linear clustered plug nozzle with round-to-square modules, Aerosp. Sci. Technol. 11 (2007) 110–118, https://doi.org/10.1016/j.ast.2006.08.004, https://www.sciencedirect.com/science/article/pii/S1270963806001143.

[18] Y. Wang, Y. Lin, Q. Eri, B. Kong, Flow and thrust characteristics of an expansion–deflection dual-bell nozzle, Aerosp. Sci. Technol. 123 (2022) 107464, https://doi.org/10.1016/j.ast.2022.107464, https://www.sciencedirect.com/science/article/pii/S1270963822001389.

[19] Y. Wang, Q. Eri, J. Huang, B. Kong, Multi-objective aerodynamic optimization of expansion–deflection nozzle based on B-spline curves, Aerosp. Sci. Technol. 147 (2024) 109016, https://doi.org/10.1016/j.ast.2024.109016, https://www.sciencedirect.com/science/article/pii/S1270963824001494.

[20] Y. Shi, C. Yan, Y. Zhou, J. Wu, Y. Wang, S. Yu, Y. Chen, Chapter 8 - materials for four-dimensional printing, in: Y. Shi, C. Yan, Y. Zhou, J. Wu, Y. Wang, S. Yu, Y. Chen (Eds.), Materials for Additive Manufacturing, in: 3D Printing Technology Series, Academic Press, 2021, pp. 679–739, https://www.sciencedirect.com/science/article/pii/B9780128193020000080.

[21] K.G. Cooper, J.L. Lydon, M.D. LeCorre, Z.C. Jones, D.S. Scannapieco, D.L. Ellis, B.A. Lerch, Three-Dimensional Printing GRCop-42, Technical Report, NASA, 2018.

[22] P.R. Gradl, S.E. Greene, C. Protz, B. Bullard, J. Buzzell, C. Garcia, J. Wood, R. Osborne, J. Hulka, K.G. Cooper, Additive manufacturing of liquid rocket engine combustion devices: a summary of process developments and hot-fire testing results, in: 2018 Joint Propulsion Conference, American Institute of Aeronautics and Astronautics, Cincinnati, Ohio, 2018, https://arc.aiaa.org/doi/10.2514/6.2018-4625.

[23] P.R. Gradl, C.S. Protz, K. Cooper, D. Ellis, L.J. Evans, C. Garcia, GRCop-42 development and hot-fire testing using additive manufacturing powder bed fusion for channel-cooled combustion chambers, in: AIAA Propulsion and Energy 2019 Forum, American Institute of Aeronautics and Astronautics, Indianapolis, IN, 2019, https://arc.aiaa.org/doi/10.2514/6.2019-4228.

[24] G. Demeneghi, B. Barnes, P. Gradl, D. Ellis, J.R. Mayeur, K. Hazeli, Directed energy deposition GRCop-42 copper alloy: characterization and size effects, Mater. Des. 222 (2022) 111035, https://doi.org/10.1016/j.matdes.2022.111035, https://linkinghub.elsevier.com/retrieve/pii/S0264127522006578.

[25] G. Demeneghi, P. Gradl, J.R. Mayeur, K. Hazeli, GRCop-42: comparison between laser powder bed fusion and laser powder direct energy deposition, Addit. Manuf. Lett. 10 (2024) 100224, https://doi.org/10.1016/j.addlet.2024.100224, https://linkinghub.elsevier.com/retrieve/pii/S277236902400032X.

[26] G. Angelino, Approximate method for plug nozzle design, AIAA J. 2 (1964) 1834–1835, https://doi.org/10.2514/3.2682, https://arc.aiaa.org/doi/10.2514/3.2682, publisher: American Institute of Aeronautics and Astronautics.

[27] M. Onofri, M. Calabro, G. Hagemann, H. Immich, P. Sacher, F. Nasuti, P. Reijasse, Plug nozzles: summary of flow features and engine performance - overview of RTO/AVT WG 10 subgroup 1, in: 40th AIAA Aerospace Sciences Meeting & Exhibit, Aerospace Sciences Meetings, American Institute of Aeronautics and Astronautics, 2002, https://arc.aiaa.org/doi/10.2514/6.2002-584.

[28] L. Fadigati, F. Rossi, N. Souhair, V. Ravaglioli, F. Ponti, Development and simulation of a 3D printed liquid oxygen/liquid natural gas aerospike, Acta Astronaut. 216 (2024) 105–119, https://doi.org/10.1016/j.actaastro.2023.12.037, https://www.sciencedirect.com/science/article/pii/S0094576523006677.

[29] K. Chutkey, M. Viji, S.B. Verma, Effect of clustering on linear plug nozzle flow field for overexpanded internal jet, Shock Waves 27 (2017) 623–633, https://doi.org/10.1007/s00193-017-0707-y.

[30] M.D. Gagliardi, L. Fadigati, N. Souhair, F. Ponti, Validation of a numerical strategy to simulate the expansion around a plug nozzle, in: Materials Research Proceedings, vol. 37, Materials Research Forum LLC, Padova, 2023, pp. 695–698, https://www.mrforum.com/product/9781644902813-148.

[31] E.F. Toro, The HLLC Riemann solver, Shock Waves 29 (2019) 1065–1082, https://doi.org/10.1007/s00193-019-00912-4.

[32] F.R. Menter, Two-equation eddy-viscosity turbulence models for engineering applications, AIAA J. 32 (1994) 1598–1605, https://doi.org/10.2514/3.12149, https://arc.aiaa.org/doi/10.2514/3.12149, publisher: American Institute of Aeronautics and Astronautics.

[33] F.R. Menter, M. Kuntz, R. Langtry, Ten years of industrial experience with the SST turbulence model, in: Turbulence, Heat, and Mass Transfer, Turbulence, Heat and Mass Transfer, Begell House, Antalya, Turkey, 2003, pp. 625–632.

[34] S. Gordon, B.J. McBride, Computer Program for Calculation of Complex Chemical Equilibrium Compositions and Applications I. Analysis, NASA Reference Publication, 1994, https://ntrs.nasa.gov/citations/19950013764.

[35] B.J. McBride, S. Gordon, Computer Program for Calculation of Complex Chemical Equilibrium Compositions and Applications II. Users Manual and Program Description, NASA Reference Publication, 1996, http://akrmys.com/public/cea/doc/xRP-1311P2.pdf.

[36] Bonnie J. McBride, Sanford Gordon, Lewis Research Center Cleveland, Ohio, 1992, NASA Reference Publication, http://akrmys.com/public/cea/doc/xRP-1271.pdf.

[37] P.P. Nair, A. Suryan, H.D. Kim, Computational study on flow through truncated conical plug nozzle with base bleed, Propuls. Power Res. 8 (2019) 108–120, https://doi.org/10.1016/j.jppr.2019.02.001, https://linkinghub.elsevier.com/retrieve/pii/S2212540X19300112.

[38] S. Soman, A. Suryan, P.P. Nair, H. Dong Kim, Numerical analysis of flowfield in linear plug nozzle with base bleed, J. Spacecr. Rockets 58 (2021) 1786–1798, https://doi.org/10.2514/1.A34992, publisher: American Institute of Aeronautics and Astronautics, https://arc.aiaa.org/doi/10.2514/1.A34992.

[39] B. Zang, U.S. Vevek, N. Tze How D, OpenFOAM based numerical simulation study of an underexpanded supersonic jet, in: AIAA SciTech Forum, American Institute of Aeronautics and Astronautics, 2017, https://arc.aiaa.org/doi/10.2514/6.2017-0747.

[40] H. Babinsky, J.K. Harvey (Eds.), Shock Wave-Boundary-Layer Interactions, Cambridge Aerospace Series, Cambridge University Press, Cambridge, 2011, https://www.cambridge.org/core/books/shock-waveboundarylayer-interactions/1EC84B4EBF65B1B20C0CA60806B7DFF5.

[41] Y. Weng, Q. Li, G. Tan, W. Su, Y. You, Numerical investigations on interactions between 2D/3D conical shock wave and axisymmetric boundary layer at Ma = 2.2, Aerosp. Sci. Technol. 144 (2024) 108769, https://doi.org/10.1016/j.ast.2023.108769, https://www.sciencedirect.com/science/article/pii/S127096382300665X.

[42] A. Gross, J. Little, H.F. Fasel, Numerical investigation of unswept and swept turbulent shock-wave boundary layer interactions, Aerosp. Sci. Technol. 123 (2022) 107455, https://doi.org/10.1016/j.ast.2022.107455, https://www.sciencedirect.com/science/article/pii/S1270963822001298.

[43] J. Délery, J.-P. Dussauge, Some physical aspects of shock wave/boundary layer interactions, Shock Waves 19 (2009) 453–468, https://doi.org/10.1007/s00193-009-0220-z.

[44] Y. Yang, Y. Zhang, H. Chen, Analysis and manipulation of the separation zone in an overexpanded combined exhaust nozzle, Aerosp. Sci. Technol. 135 (2023) 108196, https://doi.org/10.1016/j.ast.2023.108196, https://www.sciencedirect.com/science/article/pii/S1270963823000937.

[45] M. He, L. Qin, Y. Liu, Numerical investigation of flow separation behavior in an over-expanded annular conical aerospike nozzle, Chin. J. Aeronaut. 28 (2015) 983–1002, https://doi.org/10.1016/j.cja.2015.06.016, https://www.sciencedirect.com/science/article/pii/S1000936115001223.

[46] G. Hagemann, M. Frey, Shock pattern in the plume of rocket nozzles: needs for design consideration, Shock Waves 17 (2008) 387–395, https://doi.org/10.1007/s00193-008-0129-y.

[47] W.J. Bannik, E.M. Houtman, M.M.J. Schoones, On the interaction between a linear plug nozzle exhaust flow \ & supersonic external flow, in: Aerothermodynamics for Space Vehicles, in: ESA Special Publication, vol. 426, 1999, p. 403, https://ui.adsabs.harvard.edu/abs/1999ESASP.426..403B.

[48] K. Chutkey, B. Vasudevan, N. Balakrishnan, Analysis of annular plug nozzle flowfield, J. Spacecr. Rockets 51 (2014) 478–490, https://doi.org/10.2514/1.A32617, https://arc.aiaa.org/doi/10.2514/1.A32617.

[49] P.K. Chang, Separation of Flow, Pergamon, 1970.

[50] J.L. Herrin, J.C. Dutton, Supersonic base flow experiments in the near wake of a cylindrical afterbody, AIAA J. 32 (1994) 77–83, https://doi.org/10.2514/3.11953, https://arc.aiaa.org/doi/10.2514/3.11953.

[51] F. Nasuti, M. Onofri, Theoretical analysis and engineering modeling of flowfields in clustered module plug nozzles, J. Propuls. Power 15 (1999) 544–551, https://doi.org/10.2514/2.5477, publisher: American Institute of Aeronautics and Astronautics, https://arc.aiaa.org/doi/10.2514/2.5477.

[52] Additive Manufacturing LLC, GRCop-42 product information, Datasheet, 2023.

[53] D.S. Scannapieco, J.J. Lewandowski, R.B. Rogers, D.L. Ellis, In-Situ Alloying of GRCop-42 via Additive Manufacturing: Precipitate Analysis, 2020.

Luca Fadigati is currently a P.h.D. candidate at the University of Bologna in Mechanics and Advanced Engineering Sciences. He earned his Banchelor and Master of Science in Aerospace Engineering at the University of Bologna. He did an internship of three months at the Department of Information Technology, University of Uppsala. His main research is focusses on simulation of thermal protection of solid rocket engine and numerically investigating the performance of an aerospike engine.

Ernesto Sozio is currently a Senior Propulsion Aerodynamics Engineer at Pangea Aerospace. He earned both his B.S. and M.S. degrees in Mechanical Engineering from Polytechnic University of Bari, with a specialization in Propulsion. He received a Post-Graduate Research Master from the von Karman Institute for Fluid Dynamics with a specialization in Turbomachinery and Propulsion. He worked 3 years for Alstom Power in Switzerland, firstly as Development Engineer Thermals and later as Turbine Aerodynamic Design and Performance Engineer, participating at the design and development of a heavy-duty gas turbine for power generation applications. Later he joined GE - Avio Aero in Italy as Turbine Aerodynamic Lead Engineer where he spent more than 6 years, and he was in charge of the aero design of several turbines for aeronautical applications. He finally joined Pangea Aerospace (Spain) in 2022 as Turbomachinery Fluid Dynamics Engineer, and later promoted to the role of Senior Propulsion Aerodynamics Engineer. He is currently project leader of the performance improvement of aerospike engines, and leader of the fluid dynamics design of pumps and turbines for Liquid Rocket Engine (LRE) applications.

Federico Rossi holds a B.Sc. and M.Sc. in Aerospace Engineering from the University of Bologna, and a Second Level Master's Degree by the University of Rome "La Sapienza" in Space Transportation Systems and Reentry Vehicles. After working 1 year at Avio in the Cryogenic Propulsion group, he co-founded Pangea Aerospace in 2018. Since then, he has been serving as Head of Propulsion at the company, leading the team and all the company's propulsion developments. Notably DemoP1, the first LOX/LNG aerospike engine to be hot-fired in the world; Arcos, a 300 kN thrust class aerospike platform; and U-Nyx, a 1 N-thrust HTP-based bipropellant satellite propulsion system.

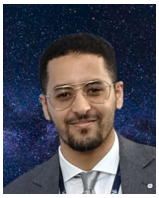

Nabil Souhair has a MSc and a PhD in Aerospace Engineering and Mechanics and Advanced Science of Engineering respectively, from the University of Bologna. He is currently Assistant Professor in Aerospace Propulsion at the International University of Rabat and Adjunct Professor at the University of Bologna where he cooperates with the Alma Propulsion Laboratory. His main research interests are Electric Propulsion, Plasma Thrusters, in-space propulsion systems, Space transportation and Aerospikes, with a focus on modeling and performance characterization.

Fabrizio Ponti received his PhD in Machine Engineering from Polytechnic of Bari, Italy, in 2001. He is currently Full Professor in Aerospace Propulsion at the University of Bologna since 2018, teaching at the Master in Aerospace Engineering. His main research interests are Solid Rocket Boosters simulation and modelling with particular focus on 3D modelling of the burn-back process, thermal protection ablation, internal ballistics, and flaws modelling. He is also involved in Aerospike performance evaluation and modelling with focus on the simulation of the flow characteristics and the engine design optimization. He is also involved in research topics such as the modelling of the combustion process in internal combustion engines and gas turbines, and the development and modelling of electric propulsion systems.